INTERNATIONAL JOURNAL OF
NUMERICAL ANALYSIS AND MODELING
Volume 21, Number 6, Pages 850–878

doi: 10.4208/ijnam2024-1034

AN EFFICIENT ROTATIONAL PRESSURE-CORRECTION SCHEME FOR THE 2D/3D NAVIER-STOKES/DARCY COUPLING PROBLEM

MINTING ZHAO[1], JIAWEI GAO[2,*], MD. ABDULLAH AL MAHBUB[3], AND DAN CHEN[4,*]

Abstract. This article proposes and analyzes a rotational pressure-correction method for the Navier-Stokes/Darcy(NSD) system with Beavers-Joseph-Saffman-Jones interface conditions. This method mainly solves the Navier-Stokes/Darcy problem in two steps. The first step is the viscous step. The intermediate velocity can be obtained after the pressure gradient is explicitly processed by the algorithm. The second step is the projection step, which first projects the intermediate velocity onto a divergence-free space, and then corrects the velocity and pressure. The main advantage of these methods is that they have first/second order accuracy and do not have the incompressibility constraint of NSD system. For solving the Navier-Stokes equations, each time step requires only one vector-valued elliptic equation and one scalar-valued Poisson equation. Therefore, this method has high computational efficiency. Compared with other traditional related methods, this method is no longer affected by any artificial boundary conditions, and can achieve the optimal convergence order. Finally, unconditional stability and long time stability are established. 2D/3D numerical experiments are presented to illustrate the features of the proposed method and verify the results of the theoretical analysis.

Key words. First-order/second-order temporal scheme, rotational pressure-correction scheme, Navier-Stokes/Darcy system, stability, 2D/3D numerical experiments.

1. Introduction

The NSD system is one of the classical equations of fluid mechanics, because it describes the physical phenomena of fluid motion. It may be used to simulate surface water flow, subsurface oil and groundwater flow, as well as flow in porous media, such as [1, 2, 3, 4, 5]. Due to the coupling of free flow and flow in porous media, the complex geometric shape of free flow, refined space-time scale, strong heterogeneity of physical parameters and uncertainty of experimental data, the mathematical research of this system has always been a very difficult challenge.

In most important applications, it is difficult to solve the exact solution of multi-domain, multi-physics field coupled NSD system. Therefore, the efficient numerical solution of the system is particularly important. Most methods are designed for the development of an approximate solution to the NSD system, including coupled finite element methods [2, 6, 7, 8, 9, 10, 11], domain decomposition methods [12, 13, 14, 15, 16, 17, 18, 19, 20, 21], Lagrange multiplier methods [22, 23], two-grid methods [5, 24], implicit-explicit method [25, 26, 27, 28], discontinuous Galerkin methods [29, 30, 31, 32, 33], mortar discretizations [34, 35, 36], boundary integral methods [37, 38], and others [39, 40, 41, 42, 43, 44, 45]. These numerical methods have been widely devoted to achieve their required accuracy in certain practice. While they have proven to be very successful, a theory to ensure their long time stability is still being developed. In recent years, some efficient second-order (in time) accurate methods have been developed and investigated for a NSD system [42, 46]. These methods establish an unconditional and uniform stability and further

Received by the editors on January 25, 2024 and, accepted on July 12, 2024.
2000 *Mathematics Subject Classification.* 35J20, 65N08, 76D05.
*Corresponding authors.

lead to a uniform control of errors, which is highly desirable for modeling many physical processes. In particular, two second-order time method for coupled NSD systems and optimal theoretical results are studied in [46]. These results provide a theoretical support for second-order large time step method for the NSD system.

It is well known that a lot of difficulties are arising from the coupled system: the mixed nonlinear problem, their shared rigid interface, the energy dissipation derived from a decoupling strategy, and their complex system existing in itself. Thus, it is not easy to solve efficiently the coupled system with the Navier-Stokes equations because of the saddle point structure induced by the incompressibility constraint [47, 48, 49, 50, 51, 52]. For the past few years, a projection method has attracted more and more attention from researchers because of its simplicity and efficiency[53, 54, 55, 56]. The projection algorithm[57] has undergone some evolution and has been well further developed. Firstly, Chorin-Temam's algorithm was improved by making the pressure explicit in the viscous step and by correcting it in the projection step. Hereafter, the same fundamental idea of decomposing vector fields into a divergence-free part and a gradient has remained effective for solving the Navier-Stokes equations [58, 59]. For incompressible flow, it is effective to decouple the system of pressure from that of velocity by using the projection method [60]. These methods usually consist of two substeps. One substep explicitly satisfies the Laplacian expression of the velocity or pressure gradient, and the other substep implicitly corrected . In [61], the author gives a second order in time incremental pressure correction finite element method for the Navier-Stokes/Darcy problem. In this method, the Navier-Stokes/Darcy problem is solved in three steps: a convection-diffusion step, a projection correction (incremental pressure correction) step and a Darcy step. In [62], a first order linearized pressure correction projection method is proposed and analyzed for the time-dependent diffusive Peterlin viscoelastic model, which can describe the unsteady behavior of some incompressible polymeric fluids in two dimensions. Details on the various projection method can be found at [63, 64, 65, 66].

Here, we restrict ourselves to the rotational pressure-correction method for the NSD system. The most challenging issue is how to develop the proper rotational pressure-correction method. One of the main difficulties in decoupling the coupled system related to the incompressible flow is that this system has a complicated boundary condition. Most of these schemes imply an artificial condition not satisfied by the exact pressure, which induces a numerical boundary layer, and, in turn, results in a loss of accuracy. In addition to the complexity of the coupling problem, the analysis of nonlinear terms for the incompressible Navier-Stokes equation is another difficulty, and we need to pay attention to the analysis skills to overcome it. The projection method has been widely used because of its efficiency and simplicity. However, the rigorous error analysis of coupled systems with incompressible Navier-Stokes equations still needs further study.

In this article, based on the key idea of the rotational pressure-correction method for the Stokes problem with an open boundary condition in [66, 67], we propose and rigorously analyze this scheme to solve the coupled NSD system. A first-order backward Euler and second-order backward difference formulas are utilized to discretize the time derivative while the finite elements are used to treat the spatial discretization. The central advantage of our approach is a time-dependent version of domain decomposition, and has first-order/second-order accuracy without the incompressibility constraint in the Navier-Stokes system. Moreover, the negative

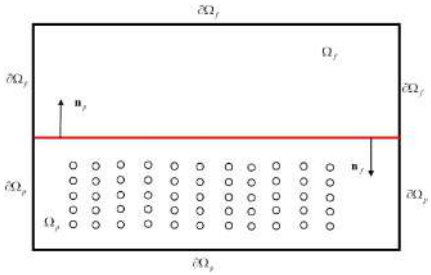

FIGURE 1. The global domain Ω consists of free fluid flow subdomain Ω_f and porous media fluid flow subdomain Ω_p, separated by a common interface Γ.

effect of an artificial boundary condition has been eliminated and numerical precision is furthermore guaranteed. The main feature of these methods are that we only solve one vector-valued elliptic problem and one scalar-valued Poisson problem per time step. Thus, the cost of these algorithms is dominant to solve the (quasi-)Poisson equation, especially for large size problems. Finally, the unconditional stability and long time stability of the NSD system are proved. The accuracy of the theory is verified by 2D/3D numerical experiments.

The rest of the paper is organized as follows. In section 2, we introduce the fluid-fluid model using the NSD system. In section 3, a lemma used in the analysis is given. In section 4, the first-order/second-order time discretizations of rotational pressure-correction methods are introduced. The unconditional stability and long time stability of NSD system are strictly proved. In section 5, the fully discrete scheme of NSD system is given. Finally, three numerical experiments are given to demonstrate the effectiveness of the proposed method.

2. Preliminary

In this section, we begin with a brief introduction to the model. To specify the problem considered, let the two domains in $R^d, d = 2, 3$, be denoted by Ω_p and Ω_f and lie across an interface Γ from each other (see Figure 1). We can simplify the model to the following situation. The coupled NSD problem is stated as follows:

$$S\frac{\partial \phi}{\partial t} - \nabla \cdot (\mathbb{K}\nabla\phi) = f, \text{ in } \Omega_p, \tag{1}$$

$$\phi = 0, \text{ on } \partial\Omega_p \backslash \Gamma, \tag{2}$$

$$\frac{\partial \mathbf{u}}{\partial t} - \nabla \cdot \mathbb{T}(\mathbf{u}, p) + (\mathbf{u} \cdot \nabla)\mathbf{u} = \mathbf{f}, \text{ in } \Omega_f, \tag{3}$$

$$\nabla \cdot \mathbf{u} = 0, \text{ in } \Omega_f, \tag{4}$$

$$\mathbf{u} = 0, \text{ on } \partial\Omega_f \backslash \Gamma, \tag{5}$$

where $\mathbf{u}_p = -\mathbb{K}\nabla\phi$ is the fluid velocity discharge rate, S is the the water storage coefficient, $\mathbb{K}$ is the hydraulic conductivity tensor, and f is the sink/source term; $\phi = z_0 + \frac{p_D}{\rho g}$ denotes the hydraulic head, where p_D denotes the dynamic pressure, and z_0, ρ, g are the height, density, and the gravity constant, respectively. In the free-flow region Ω_f, let $\mathbf{u}$ denote the fluid velocity, p the kinematic pressure, $\mathbf{f}$ the external body force, and μ below the kinematic viscosity of the fluid. Additionally, $\mathbb{T}(\mathbf{u}, p) = 2\mu\mathbb{D}(\mathbf{u}) - p\mathbb{I}$ is the stress tensor. $\mathbb{D}(\mathbf{u}) = \frac{1}{2}\left(\nabla\mathbf{u} + \nabla^T\mathbf{u}\right)$ is the deformation tensor. $\mathbb{I}$ is the identity tensor.

On the interface Γ, we have prescribed the following Beavers-Joseph-Saffman-Jones interface conditions [68, 69, 70]

$$\mathbf{u}\cdot\mathbf{n}_f=\mathbf{u}_p\cdot\mathbf{n}_f=-(\mathbb{K}\nabla\phi)\cdot\mathbf{n}_f, \tag{6}$$

$$-\tau_j\cdot(\mathbb{T}(\mathbf{u},p)\cdot\mathbf{n}_f)=\alpha_0\tau_j\cdot\mathbf{u},\quad j=1,\cdots,d-1, \tag{7}$$

$$-\mathbf{n}_f\cdot(\mathbb{T}(\mathbf{u},p)\cdot\mathbf{n}_f)=g\phi, \tag{8}$$

where α_0 is the Beavers-Joseph-Saffman-Jones coefficient, n_f denotes the outer unit normal vector for the free flow and $\tau_j, j=1,2,\cdots,d-1$ denotes a linearly independent set of vectors tangent to the interface Γ.

The system (2.1)-(2.5) is considered in conjunction with the following initial

$$\phi(0,x)=\phi_0(x),\ \text{in}\ \Omega_p, \tag{9}$$

$$\mathbf{u}_S(0,x)=\mathbf{u}_0(x),\ \text{in}\ \Omega_f, \tag{10}$$

where $x=(x_1,x_2,\cdots x_d)$.

For the convenience of later analysis, we introduce some notation that will be used later. Let $\mathbf{X}_f^{'}$ and $X_p^{'}$ denote the dual spaces of $\mathbf{X}_f$ and X_p, respectively. $(\cdot,\cdot)_D$ denotes the L^2 inner product in the domain $D(D=\Omega_f$ or $\Omega_p)$ and $\langle\cdot,\cdot\rangle$ denotes the L^2 inner product on the interface Γ. Here, we define the norms $\|\phi\|_\Gamma=\langle\phi,\phi\rangle^{1/2},\forall\phi\in X_p$, $\|\vec{\mathbf{v}}\|_\Gamma=\left(\|\mathbf{v}\cdot\mathbf{n}\|_\Gamma^2+\|\mathbf{v}\cdot\tau\|_\Gamma^2+\|\psi\|_\Gamma^2\right)^{1/2}$ and $\|\vec{\mathbf{v}}\|_S=\langle\langle\vec{\mathbf{v}},\vec{\mathbf{v}}\rangle\rangle^{1/2},\forall\vec{\mathbf{v}}=[\mathbf{v},\psi]^T$. We have that $\|\cdot\|_S$ is equivalent to the L^2 norm, i.e., $\|\cdot\|_S\sim\|\cdot\|_0$. In order to derive the variational formulation for the model problem(1)-(5), we define the following Hilbert spaces [71]:

$$\begin{aligned}\mathbf{X}_f&=\left\{\mathbf{v}\in[H^1(\Omega_f)]^d:\ \mathbf{v}=0\ \text{on}\ \partial\Omega_f\setminus\Gamma\right\},\\ X_p&=\left\{\psi\in H^1(\Omega_p):\ \psi=0\ \text{on}\ \partial\Omega_p\setminus\Gamma\right\},\\ \overline{\mathbf{X}}&=\mathbf{X}_f\times X_p,\ M_f=L^2(\Omega_f)\cap H^1(\Omega_f).\end{aligned}$$

We recall the following vector formulas

$$\begin{aligned}\langle\langle\vec{\mathbf{u}}_t,\vec{\mathbf{v}}\rangle\rangle=&(\mathbf{u}_t,\mathbf{v})_{\Omega_f}+gS(\phi_t,\psi)_{\Omega_p},\\ a(\vec{\mathbf{u}},\vec{\mathbf{v}})=&2\mu(\mathbb{D}(\mathbf{u}),\mathbb{D}(\mathbf{v}))_{\Omega_f}+g(\mathbb{K}\nabla\phi,\nabla\psi)_{\Omega_p}+\alpha_0\langle\mathbf{u}\cdot\tau,\mathbf{v}\cdot\tau\rangle,\\ a_\Gamma(\vec{\mathbf{u}},\vec{\mathbf{v}})=&g\langle\phi,\mathbf{v}\cdot\mathbf{n}_f\rangle_\Gamma-g\langle\mathbf{u}\cdot\mathbf{n}_f,\psi\rangle_\Gamma,\\ (\vec{\mathbf{f}},\vec{\mathbf{v}})=&(\mathbf{f},\mathbf{v})_{\Omega_f}+g(f,\psi)_{\Omega_p},\\ b(\vec{\mathbf{v}},q)=&(\mathrm{div}\mathbf{v},q)_{\Omega_f},\end{aligned}$$

where $\vec{\mathbf{u}}=[\mathbf{u},\phi]^T,\vec{\mathbf{v}}=[\mathbf{v},\psi]^T,\vec{\mathbf{f}}=[\mathbf{f},gf]^T$.

The trilinear form is defined as: $\forall(\mathbf{u},\mathbf{w},\mathbf{v})\in\mathbf{X}_f\times\mathbf{X}_f\times\mathbf{X}_f$,

$$C(\mathbf{u},\mathbf{w},\mathbf{v})=(\mathbf{u}\cdot\nabla\mathbf{w},\mathbf{v})_{\Omega_f}. \tag{11}$$

Especially, these bilinear forms satisfy the following coercive property [7]:

$$a(\vec{\mathbf{u}},\vec{\mathbf{u}})\geq(\mu\|\nabla\mathbf{u}\|_0^2+gK_{min}\|\nabla\phi\|_0^2+\alpha_0\|\mathbf{u}\cdot\tau\|_\Gamma^2)\geq C_a\|\nabla\vec{\mathbf{u}}\|_0^2, \tag{12}$$

$$a_\Gamma(\vec{\mathbf{u}},\vec{\mathbf{u}})=0. \tag{13}$$

where $C_a=\min(\mu,gK_{min},\alpha_0)>0$, K_{min} is the minimum eigenvalue of $\mathbb{K}$, and $L^2(\Omega)$ and $L^2(\Gamma)$ are equipped with the norms $\|\cdot\|_0$ and $\|\cdot\|_\Gamma$, respectively.

Finally, we introduce the continuous variational form of the problem (1)-(5). Multiplying (1)-(5) by $g\psi\in X_p$ and $(\mathbf{v},q)\in\mathbf{X}_f\times M_f$, integrating over the corresponding domains and applying the divergence theorem, we find $(\vec{\mathbf{u}},p)\in(\overline{\mathbf{X}},M_f)$

with $\phi_t \equiv \frac{\partial \phi}{\partial t} \in X_p^{'}$ and $\mathbf{u}_t \equiv \frac{\partial \mathbf{u}}{\partial t} \in \mathbf{X}_f^{'}$ for given $f \in X_p$ and $\mathbf{f} \in \mathbf{X}_f$ such that, for $\forall(\vec{\mathbf{v}}, q) \in \overline{\mathbf{X}} \times M_f$,

$$\langle\langle \vec{\mathbf{u}}_t, \vec{\mathbf{v}} \rangle\rangle + a(\vec{\mathbf{u}}, \vec{\mathbf{v}}) - b(\mathbf{v}, p) + b(\mathbf{u}, q) + a_\Gamma(\vec{\mathbf{u}}, \vec{\mathbf{v}}) + C(\mathbf{u}, \mathbf{u}, \mathbf{v}) = (\vec{\mathbf{f}}, \vec{\mathbf{v}}). \tag{14}$$

More detailed results regarding to the problems of (1)-(10) can be found in [2, 68, 69].

3. The nonlinear property

In this section, we will analyze the stability of the presented method related to the nonlinear property. Under the classical technique of the coupled problems related to the Navier-Stokes system, the existence and uniqueness of the corresponding coupled NSD problems presented can be obtained. Our main aim is to show the stability of the weak solution in continuous system, which also can be obtained for the discrete finite element system.

Then, we can obtain the following result.

Lemma 3.1. [76] *Assume that* $\mathbf{u}$ *satisfies the following smallness condition*

$$\|\nabla \mathbf{u}\|_0 \leq \frac{C_a}{8C_0}, \ \forall t \in [0, T]. \tag{15}$$

Then, we have

$$|C(\mathbf{u}, \mathbf{v}, \mathbf{w})| \leq \frac{C_a}{8} \|\nabla \mathbf{v}\|_0 \|\nabla \mathbf{w}\|_0, \forall \mathbf{u}, \mathbf{v}, \mathbf{w} \in \mathbf{X}_f \ \textit{and} \ t \in [0, T], \tag{16}$$

Proof. Using the assumption (15), we can estimate the trilinear term $C(\cdot, \cdot, \cdot)$ as follows

$$C(\mathbf{u}, \mathbf{v}, \mathbf{w}) \leq C_0 \|\nabla \mathbf{u}\|_0 \|\nabla \mathbf{v}\|_0 \|\nabla \mathbf{w}\|_0 \leq \frac{C_a}{8} \|\nabla \mathbf{v}\|_0 \|\nabla \mathbf{w}\|_0. \quad \square \tag{17}$$

4. Time discretization and stability

In this section, we show the rotational pressure-correction method in [60] for approximating the Navier-Stokes equations with complex boundary conditions. Here we will consider two different numerical schemes to solve the system: One is the so-called BE (backward Euler scheme), which is first-order accurate with respect to Δt. Anther one is the so-called BDF2 (backward difference formulas scheme) with second-order accurate with respect to Δt.

There are generally many ways to discretize the time-dependent NSD equations in time. Several finite element methods are available for the numerical solution of the system. For convenience, let us introduce the following notation. We denote the real positive parameter $\Delta t = t^{k+1} - t^k, k = 0, 1, 2 \cdots$, represents the discretization step, while the super-index k indicates that the quantity under consideration refers to the time t^k. First, we study the rotational pressure-correction method by using BE.

4.1. The BE rotational pressure-correction method.

For any $\vec{\mathbf{u}}^k \equiv (\mathbf{u}^k, \phi^k) \in \bar{X}$, $\Delta t > 0$, find $\tilde{\vec{\mathbf{u}}}^{k+1} \equiv (\tilde{\mathbf{u}}^{k+1}, \phi^{k+1}) \in \overline{\mathbf{X}}$ such that

$$\begin{aligned} &\left\langle\left\langle \frac{D^1 \tilde{\vec{\mathbf{u}}}^{k+1}}{\Delta t}, \vec{\mathbf{v}} \right\rangle\right\rangle + a\left(\tilde{\vec{\mathbf{u}}}^{k+1}, \vec{\mathbf{v}}\right) - b\left(\mathbf{v}, p^k\right) + a_\Gamma\left(\vec{\mathbf{u}}^k, \vec{\mathbf{v}}\right) \\ &\qquad + C\left(\mathbf{u}^k, \tilde{\mathbf{u}}^{k+1}, \mathbf{v}\right) = \left(\vec{\mathbf{f}}^{k+1}, \vec{\mathbf{v}}\right), \quad \forall \vec{\mathbf{v}} \in \overline{\mathbf{X}}, \end{aligned} \tag{18}$$

where $D^1 \tilde{\vec{\mathbf{u}}}^{k+1} = \tilde{\vec{\mathbf{u}}}^{k+1} - \vec{\mathbf{u}}^k$ denotes the difference operator.

Subsequently, compute $\left(\mathbf{u}^{k+1}, z^{k+1}\right) \in \mathbf{X}_f \times M_f$ such that

$$\frac{\mathbf{u}^{k+1} - \tilde{\mathbf{u}}^{k+1}}{\Delta t} + \nabla z^{k+1} = 0, \qquad \text{in } \Omega_f, \tag{19}$$

$$\mathrm{div}\mathbf{u}^{k+1} = 0, \qquad \text{in } \Omega_f, \tag{20}$$

$$\mathbf{u}^{k+1} \cdot \mathbf{n}|_{\partial\Omega_f \setminus \Gamma} = 0, \text{and } z^{k+1}|_{\Gamma} = 0. \tag{21}$$

Furthermore, we update p^{k+1} and $\mathbf{u}^{k+1}$ by:

$$\begin{aligned} p^{k+1} &= p^k + z^{k+1} - \chi\mu \mathrm{div}\tilde{\mathbf{u}}^{k+1}, \\ \mathbf{u}^{k+1} &= \tilde{\mathbf{u}}^{k+1} - \Delta t \nabla z^{k+1}, \end{aligned} \tag{22}$$

where the positive constant $\chi > 0$ is a given parameter before the computation phase begins.

Remark 4.1. In this algorithm, the Beavers-Joseph-Saffman-Jones interface conditions are actually imposed in the interface term $a_\Gamma(\cdot,\cdot)$, which is a bilinear term, and can be treated via a simple quantity refer to the previous time t^k. Moreover, the trilinear term $C(\cdot,\cdot,\cdot)$ is linearized by the Picard scheme.

To prove the stability of the BE scheme, we first estimate the preliminary results of the interface terms, as well as some other important terms, which are necessary and important for the proof of the algorithm. For convenience, some mathematical notations are defined:

$$\delta a^{k+1} = a^{k+1} - a^k.$$

Then, the following result follows from the basic analysis of BE scheme to discretize the time derivative [66].

Lemma 4.2. *It holds that*

$$\begin{aligned} &\|\delta\mathbf{u}^{k+1}\|_0^2 + \Delta t^2 \|\nabla z^{k+1}\|_0^2 \\ &+ \chi\mu\Delta t \left(\|\mathrm{div}\tilde{\mathbf{u}}^{k+1}\|_0^2 - \|\mathrm{div}\tilde{\mathbf{u}}^{k}\|_0^2\right) + 2\Delta t b\left(\delta\tilde{\mathbf{u}}^{k+1}, \delta p^k\right) \\ =&\|\delta\tilde{\mathbf{u}}^{k+1}\|_0^2 + \Delta t^2 \|\nabla z^{k}\|_0^2 + \chi\mu\Delta t \|\mathrm{div}\delta\tilde{\mathbf{u}}^{k+1}\|_0^2. \end{aligned} \tag{23}$$

For convenience, define the positive constant

$$\alpha = \frac{32 C_{ct}^4 C_{tr}^8}{C_a^3} > 0$$

and set $\|\vec{\mathbf{u}}\|_i^2 = \|\mathbf{u}\|_i^2 + \|\phi\|_i^2, i = 0, 1$. To avoid irrelevant technicalities, we assume that there is no external driving force, i.e., $\vec{\mathbf{f}} = \vec{\mathbf{0}}$.

Based on the previous lemmas, we can obtain the following unconditional stability and the long time stability for the transient NSD equations by using the BE rotational pressure-correction scheme.

Theorem 4.3. *(***Unconditional stability***) Under the assumption of Lemma 4.2, let $T > 0$ be any fixed time. Then, the scheme* (18)-(22) *is unconditionally stable on* $(0, T]$.

Proof. Taking the operator δ on system (18) and substituting the test function $\vec{\mathbf{v}} = 2\Delta t \delta\tilde{\vec{\mathbf{u}}}^{k+1}$ to obtain the following control of the time increments of the errors

$$\begin{aligned} &2\left(\delta\tilde{\vec{\mathbf{u}}}^{k+1}, \delta\tilde{\vec{\mathbf{u}}}^{k+1} - \delta\vec{\mathbf{u}}^{k}\right) + 2\Delta t a\left(\delta\tilde{\vec{\mathbf{u}}}^{k+1}, \delta\tilde{\vec{\mathbf{u}}}^{k+1}\right) \\ &- 2\Delta t b\left(\delta\tilde{\mathbf{u}}^{k+1}, \delta p^k\right) + 2\Delta t a_\Gamma\left(\delta\vec{\mathbf{u}}^{k}, \delta\tilde{\vec{\mathbf{u}}}^{k+1}\right) \\ &+ 2\Delta t C\left(\mathbf{u}^{k-1}, \delta\tilde{\mathbf{u}}^{k+1}, \delta\tilde{\mathbf{u}}^{k+1}\right) + 2\Delta t C\left(\delta\mathbf{u}^{k}, \tilde{\mathbf{u}}^{k+1}, \delta\tilde{\mathbf{u}}^{k+1}\right) = 0. \end{aligned} \tag{24}$$

Using the Cauchy-Schwarz inequality, yields

$$a_\Gamma(\vec{\mathbf{u}},\vec{\mathbf{v}}) \le C_{ct}\|\vec{\mathbf{u}}\|_\Gamma\|\vec{\mathbf{v}}\|_\Gamma,\ \forall \vec{\mathbf{u}},\vec{\mathbf{v}} \in \overline{\mathbf{X}}, \tag{25}$$

where C_{ct} is a positive constant depending on $\sqrt{2}g$ [7]. Furthermore, applying the trace inequality

$$\|\vec{\mathbf{v}}\|_\Gamma \le C_{tr}\|\vec{\mathbf{v}}\|_0^{1/2}\|\nabla\vec{\mathbf{v}}\|_0^{1/2}, \quad \vec{\mathbf{v}} \in \overline{\mathbf{X}}, \tag{26}$$

and the Young inequality

$$a^{1/2}b^{1/2}c \le \frac{\epsilon}{4}a^2 + \frac{1}{4\epsilon^3}b^2 + \frac{\epsilon}{2}c^2, \forall \epsilon > 0, \tag{27}$$

we have

$$\begin{aligned} a_\Gamma(\delta\vec{\mathbf{u}}^k,\delta\tilde{\vec{\mathbf{u}}}^{k+1}) \le & C_{ct}\|\delta\vec{\mathbf{u}}^k\|_\Gamma\|\delta\tilde{\vec{\mathbf{u}}}^{k+1}\|_\Gamma \\ \le & C_{ct}C_{tr}^2\|\delta\vec{\mathbf{u}}^k\|_0^{1/2}\|\nabla\delta\vec{\mathbf{u}}^k\|_0^{1/2}\|\nabla\delta\tilde{\vec{\mathbf{u}}}^{k+1}\|_0 \\ \le & C_{ct}C_{tr}^2\left(\frac{\epsilon}{2}\|\nabla\delta\tilde{\vec{\mathbf{u}}}^{k+1}\|_0^2 + \frac{\epsilon}{4}\|\nabla\delta\vec{\mathbf{u}}^k\|_0^2 + \frac{1}{4\epsilon^3}\|\delta\vec{\mathbf{u}}^k\|_0^2\right). \end{aligned}$$

Then, setting $\epsilon = \frac{C_a}{4C_{tr}^2C_{ct}}$, we have

$$2\Delta t a_\Gamma(\delta\vec{\mathbf{u}}^k,\delta\tilde{\vec{\mathbf{u}}}^{k+1}) \le \frac{C_a\Delta t}{4}\|\nabla\delta\tilde{\vec{\mathbf{u}}}^{k+1}\|_0^2 + \frac{C_a\Delta t}{8}\|\nabla\delta\vec{\mathbf{u}}^k\|_0^2 + \alpha\Delta t\|\delta\vec{\mathbf{u}}^k\|_0^2. \tag{28}$$

Applying the identity $(a-b,a) = a^2 - b^2 + (a-b)^2$ and (16) to obtain

$$\begin{aligned} \|\delta\tilde{\vec{\mathbf{u}}}^{k+1}\|_0^2 - \|\delta\vec{\mathbf{u}}^k\|_0^2 + & \|\delta\tilde{\vec{\mathbf{u}}}^{k+1} - \delta\vec{\mathbf{u}}^k\|_0^2 + C_a\Delta t\|\nabla\delta\tilde{\vec{\mathbf{u}}}^{k+1}\|_0^2 - 2\Delta t b\left(\delta\tilde{\vec{\mathbf{u}}}^{k+1},\delta p^k\right) \\ & \le \frac{C_a\Delta t}{4}\|\nabla\delta\vec{\mathbf{u}}^k\|_0^2 + \alpha\Delta t\|\delta\vec{\mathbf{u}}^k\|_0^2, \end{aligned}$$

since

$$\begin{aligned} \left|C\left(\delta\mathbf{u}^k,\tilde{\mathbf{u}}^{k+1},\delta\tilde{\mathbf{u}}^{k+1}\right)\right| \le & \frac{C_a}{8}\|\nabla\delta\tilde{\mathbf{u}}^{k+1}\|_0\|\nabla\delta\mathbf{u}^k\|_0 \\ \le & \frac{C_a}{8}\|\nabla\delta\tilde{\mathbf{u}}^{k+1}\|_0^2 + \frac{C_a}{32}\|\nabla\delta\mathbf{u}^k\|_0^2 \\ \le & \frac{C_a}{8}\|\nabla\delta\tilde{\vec{\mathbf{u}}}^{k+1}\|_0^2 + \frac{C_a}{32}\|\nabla\delta\vec{\mathbf{u}}^k\|_0^2. \end{aligned} \tag{29}$$

Using (23), noting that the bilinear term $2\Delta t b(\delta\tilde{\mathbf{u}}^{k+1},\delta p^k)$ and $\Delta t\chi\|\mathrm{div}\delta\tilde{\mathbf{u}}^{k+1}\|_0^2$ are absorbed, we find that

$$\begin{aligned} & \|\delta\tilde{\vec{\mathbf{u}}}^{k+1}\|_0^2 + \|\delta\tilde{\vec{\mathbf{u}}}^{k+1} - \delta\vec{\mathbf{u}}^k\|_0^2 + \|\delta\mathbf{u}^{k+1}\|_0^2 \\ & + \Delta t^2\|\nabla z^{k+1}\|_0^2 + \chi\mu\Delta t\|\mathrm{div}\tilde{\mathbf{u}}^{k+1}\|_0^2 + \frac{3C_a\Delta t}{2}\|\nabla\delta\tilde{\vec{\mathbf{u}}}^{k+1}\|_0^2 \\ \le & \|\delta\vec{\mathbf{u}}^k\|_0^2 + \|\delta\tilde{\mathbf{u}}^{k+1}\|_0^2 + \Delta t^2\|\nabla z^k\|_0^2 + \chi\mu\Delta t\|\mathrm{div}\tilde{\mathbf{u}}^k\|_0^2 + \chi\mu\Delta t\|\mathrm{div}\delta\tilde{\mathbf{u}}^{k+1}\|_0^2 \\ & + \frac{C_a\Delta t}{4}\|\nabla\delta\vec{\mathbf{u}}^k\|_0^2 + 4\alpha\Delta t\|\delta\vec{\mathbf{u}}^k\|_0^2. \end{aligned}$$

Choosing $\chi < C_a/4d\mu$, and the estimate

$$\|\mathrm{div}\delta\tilde{\mathbf{u}}^{k+1}\|_0 \le \sqrt{d}\|\nabla\delta\tilde{\mathbf{u}}^{k+1}\|_0, \tag{30}$$

we have

$$\chi\mu\|\mathrm{div}\delta\tilde{\mathbf{u}}^{k+1}\|_0^2 \le \frac{C_a}{4}\|\nabla\delta\tilde{\mathbf{u}}^{k+1}\|_0^2 \le \frac{C_a}{4}\|\nabla\delta\tilde{\vec{\mathbf{u}}}^{k+1}\|_0^2. \tag{31}$$

Then, we can obtain

$$\begin{aligned}
&\|\delta\tilde{\vec{\mathbf{u}}}^{k+1}\|_0^2+\|\delta\tilde{\vec{\mathbf{u}}}^{k+1}-\delta\vec{\mathbf{u}}^k\|_0^2+\|\delta\mathbf{u}^{k+1}\|_0^2\\
&+\Delta t^2\|\nabla z^{k+1}\|_0^2+\chi\mu\Delta t\|\mathrm{div}\tilde{\mathbf{u}}^{k+1}\|_0^2+\frac{5C_a\Delta t}{4}\|\nabla\delta\tilde{\vec{\mathbf{u}}}^{k+1}\|_0^2\\
\leq&(1+4\alpha\Delta t)\|\delta\vec{\mathbf{u}}^k\|_0^2+\|\delta\tilde{\mathbf{u}}^{k+1}\|_0^2+\Delta t^2\|\nabla z^k\|_0^2\\
&+\chi\mu\Delta t\|\mathrm{div}\tilde{\mathbf{u}}^k\|_0^2+\frac{C_a\Delta t}{4}\|\nabla\delta\vec{\mathbf{u}}^k\|_0^2, \qquad (32)
\end{aligned}$$

which implies

$$\begin{aligned}
&\|\delta\vec{\mathbf{u}}^{k+1}\|_0^2+\|\delta\tilde{\vec{\mathbf{u}}}^{k+1}-\delta\vec{\mathbf{u}}^k\|_0^2+\Delta t^2\|\nabla z^{k+1}\|_0^2\\
&+\chi\mu\Delta t\|\mathrm{div}\tilde{\mathbf{u}}^{k+1}\|_0^2+\frac{C_a\Delta t}{4}\|\nabla\delta\tilde{\vec{\mathbf{u}}}^{k+1}\|_0^2\\
\leq&(1+4\alpha\Delta t)\|\delta\vec{\mathbf{u}}^k\|_0^2+\Delta t^2\|\nabla z^k\|_0^2+\chi\mu\Delta t\|\mathrm{div}\tilde{\mathbf{u}}^k\|_0^2+\frac{C_a\Delta t}{4}\|\nabla\delta\vec{\mathbf{u}}^k\|_0^2.
\end{aligned}$$

Thus, we complete the proof. □

Moreover, we will establish the long time stability for the presented algorithm.

Theorem 4.4. *(***Long time stability***) Assume that Lemma 4.2 and the time-step restriction* $16\alpha\Delta t<1$ *are satisfied. Then, the solution to* (18)-(22) *is uniformly bounded for all time*

$$E_{k+1}\leq E_k, \qquad (33)$$

where $E_k=\|\delta\vec{\mathbf{u}}^k\|_0^2+\Delta t^2\|\nabla z^k\|_0^2+\chi\mu\Delta t\|div\tilde{\mathbf{u}}^k\|_0^2+C_a\Delta t\|\nabla\delta\vec{\mathbf{u}}^k\|_0^2$.

Proof. Using the same approach as for Theorem 4.3. Taking the operator δ on system (18), substituting the test function $\vec{\mathbf{v}}=2\Delta t\delta\tilde{\vec{\mathbf{u}}}^{k+1}$ and applying the identity $(a-b,a)=a^2-b^2+(a-b)^2$ to obtain the following control of the time increments of the errors

$$\begin{aligned}
&\|\delta\tilde{\vec{\mathbf{u}}}^{k+1}\|_0^2-\|\delta\vec{\mathbf{u}}^k\|_0^2+\|\delta\tilde{\vec{\mathbf{u}}}^{k+1}-\delta\vec{\mathbf{u}}^k\|_0^2+2C_a\Delta t\|\nabla\delta\tilde{\vec{\mathbf{u}}}^{k+1}\|_0^2\\
&-2\Delta tb\left(\delta\tilde{\mathbf{u}}^{k+1},\delta p^k\right)+2\Delta tC\left(\mathbf{u}^{k-1},\delta\tilde{\mathbf{u}}^{k+1},\delta\tilde{\mathbf{u}}^{k+1}\right)\\
&+2\Delta tC\left(\delta\mathbf{u}^k,\tilde{\mathbf{u}}^{k+1},\delta\tilde{\mathbf{u}}^{k+1}\right)=-2\Delta ta_\Gamma\left(\delta\vec{\mathbf{u}}^k,\delta\tilde{\vec{\mathbf{u}}}^{k+1}\right). \qquad (34)
\end{aligned}$$

Choosing $\chi<C_a/8d\mu$, and the estimate

$$\|\mathrm{div}\delta\tilde{\mathbf{u}}^{k+1}\|_0\leq\sqrt{d}\|\nabla\delta\tilde{\mathbf{u}}^{k+1}\|_0, \qquad (35)$$

we have

$$\chi\mu\|\mathrm{div}\delta\tilde{\mathbf{u}}^{k+1}\|_0^2\leq\frac{C_a}{8}\|\nabla\delta\tilde{\mathbf{u}}^{k+1}\|_0^2\leq\frac{C_a}{8}\|\nabla\delta\tilde{\vec{\mathbf{u}}}^{k+1}\|_0^2. \qquad (36)$$

Also, using the same approach as for Lemma 4.1 in [72], yields

$$\begin{aligned}
&a_\Gamma\left(\delta\vec{\mathbf{u}}^k,\delta\tilde{\vec{\mathbf{u}}}^{k+1}\right)=a_\Gamma\left(\delta\vec{\mathbf{u}}^k-\delta\tilde{\vec{\mathbf{u}}}^{k+1},\delta\tilde{\vec{\mathbf{u}}}^{k+1}\right)\\
\leq&C_{ct}C_{tr}^2\|\delta\vec{\mathbf{u}}^k-\delta\tilde{\vec{\mathbf{u}}}^{k+1}\|_0^{1/2}\|\nabla\left(\delta\vec{\mathbf{u}}^k-\delta\tilde{\vec{\mathbf{u}}}^{k+1}\right)\|_0^{1/2}\|\nabla\delta\tilde{\vec{\mathbf{u}}}^{k+1}\|_0\\
\leq&C_{ct}C_{tr}^2\|\delta\vec{\mathbf{u}}^k-\delta\tilde{\vec{\mathbf{u}}}^{k+1}\|_0^{1/2}\left(\|\nabla\delta\tilde{\vec{\mathbf{u}}}^{k+1}\|_0^{1/2}+\|\nabla\delta\vec{\mathbf{u}}^k\|_0^{1/2}\right)\|\nabla\delta\tilde{\vec{\mathbf{u}}}^{k+1}\|_0\\
\leq&C_{ct}C_{tr}^2\left(\epsilon\|\delta\tilde{\vec{\mathbf{u}}}^{k+1}\|_0^2+\frac{\epsilon}{2}\|\delta\tilde{\vec{\mathbf{u}}}^{k+1}\|_0^2+\frac{\epsilon}{4}\|\delta\vec{\mathbf{u}}^{k+1}\|_0^2+\frac{1}{4\epsilon^2}\|\delta\vec{\mathbf{u}}^k-\delta\tilde{\vec{\mathbf{u}}}^{k+1}\|_0^{1/2}\right). \qquad (37)
\end{aligned}$$

Choosing $\epsilon = \frac{C_a}{8C_{tr}^2 C_{ct}}$, we have

$$\begin{aligned}
&2\Delta t a_\Gamma\left(\delta\vec{\mathbf{u}}^k, \delta\tilde{\vec{\mathbf{u}}}^{k+1}\right)\\
\leq&\frac{C_a\Delta t}{4}\|\nabla\delta\tilde{\vec{\mathbf{u}}}^{k+1}\|_0^2 + \frac{C_a\Delta t}{16}\|\nabla\delta\tilde{\vec{\mathbf{u}}}^{k+1}\|_0^2 + \frac{C_a\Delta t}{16}\|\nabla\delta\vec{\mathbf{u}}^k\|_0^2\\
&+\frac{512C_{ct}^4C_{tr}^8\Delta t}{C_a^3}\|\delta\tilde{\vec{\mathbf{u}}}^{k+1}-\delta\vec{\mathbf{u}}^k\|_0^2\\
=&\frac{5C_a\Delta t}{16}\|\nabla\delta\tilde{\vec{\mathbf{u}}}^{k+1}\|_0^2 + \frac{C_a\Delta t}{16}\|\nabla\delta\vec{\mathbf{u}}^k\|_0^2 + 16\alpha\Delta t\|\delta\tilde{\vec{\mathbf{u}}}^{k+1}-\delta\vec{\mathbf{u}}^k\|_0^2. \qquad (38)
\end{aligned}$$

Using the identity (23), the bounds (29) of the nonlinear term, and noting that the bilinear term $2\Delta t b(\delta\tilde{\mathbf{u}}^{k+1}, \delta p^k)$ and $\Delta t\chi\|\mathrm{div}\delta\tilde{\mathbf{u}}^{k+1}\|_0^2$ are absorbed, yields

$$\begin{aligned}
&\|\delta\tilde{\vec{\mathbf{u}}}^{k+1}\|_0^2 + \|\delta\tilde{\vec{\mathbf{u}}}^{k+1}-\delta\vec{\mathbf{u}}^k\|_0^2 + \|\delta\mathbf{u}^{k+1}\|_0^2 + \Delta t^2\|\nabla z^{k+1}\|_0^2\\
&+\chi\mu\Delta t\|\mathrm{div}\tilde{\mathbf{u}}^{k+1}\|_0^2 + \frac{17C_a\Delta t}{16}C_a\Delta t\|\nabla\delta\tilde{\vec{\mathbf{u}}}^{k+1}\|_0^2\\
\leq&\|\delta\vec{\mathbf{u}}^k\|_0^2 + \|\delta\tilde{\mathbf{u}}^{k+1}\|_0^2 + \Delta t^2\|\nabla z^k\|_0^2 + \chi\mu\Delta t\|\mathrm{div}\tilde{\mathbf{u}}^k\|_0^2\\
&+\frac{C_a\Delta t}{8}\|\nabla\delta\vec{\mathbf{u}}^k\|_0^2 + 16\alpha\Delta t\|\delta\tilde{\vec{\mathbf{u}}}^{k+1}-\delta\vec{\mathbf{u}}^k\|_0^2
\end{aligned}$$

which implies

$$\begin{aligned}
&\|\delta\vec{\mathbf{u}}^{k+1}\|_0^2 + (1-16\alpha\Delta t)\|\delta\tilde{\vec{\mathbf{u}}}^{k+1}-\delta\vec{\mathbf{u}}^k\|_0^2 + \Delta t^2\|\nabla z^{k+1}\|_0^2\\
&+\chi\mu\Delta t\|\mathrm{div}\tilde{\mathbf{u}}^{k+1}\|_0^2 + C_a\Delta t\|\nabla\delta\tilde{\vec{\mathbf{u}}}^{k+1}\|_0^2\\
\leq&\|\delta\vec{\mathbf{u}}^k\|_0^2 + \Delta t^2\|\nabla z^k\|_0^2 + \chi\mu\Delta t\|\mathrm{div}\tilde{\mathbf{u}}^k\|_0^2 + C_a\Delta t\|\nabla\delta\vec{\mathbf{u}}^k\|_0^2.
\end{aligned}$$

Hence, the theorem is proved since $16\alpha\Delta t < 1$. □

4.2. The BDF2 rotational pressure-correction method.

Similarly, we will introduce BDF2 and give strict stability proof. For any $\Delta t > 0$ and $\vec{\mathbf{u}}^k \equiv (\mathbf{u}^k, \phi^k) \in \overline{\mathbf{X}}$. Find $\tilde{\vec{\mathbf{u}}}^{k+1} \equiv (\tilde{\mathbf{u}}^{k+1}, \phi^{k+1}) \in \overline{\mathbf{X}}$ such that

$$\begin{aligned}
&\left\langle\left\langle\frac{D_t^2\tilde{\vec{\mathbf{u}}}^{k+1}}{2\Delta t}, v\right\rangle\right\rangle + a\left(\tilde{\vec{\mathbf{u}}}^{k+1}, \vec{\mathbf{v}}\right) - b\left(\mathbf{v}, p^k\right) + a_\Gamma\left(\sigma\vec{\mathbf{u}}^k, \vec{\mathbf{v}}\right) + C\left(\sigma\mathbf{u}^k, \tilde{\mathbf{u}}^{k+1}, \mathbf{v}\right)\\
&\qquad = \left(\vec{\mathbf{f}}^{k+1}, \vec{\mathbf{v}}\right), \quad \forall\vec{\mathbf{v}} \in \overline{\mathbf{X}}, \qquad (39)
\end{aligned}$$

where $D_t^2\tilde{\vec{\mathbf{u}}}^{k+1} = 3\tilde{\vec{\mathbf{u}}}^{k+1} - 4\vec{\mathbf{u}}^k + \vec{\mathbf{u}}^{k-1}$ and $\sigma\vec{\mathbf{u}}^k = 2\vec{\mathbf{u}}^k - \vec{\mathbf{u}}^{k-1}$.

Subsequently, compute $(\mathbf{u}^{k+1}, Z^{k+1}) \in \mathbf{X}_f \times M_f$ such that

$$\frac{3\mathbf{u}^{k+1} - 3\tilde{\mathbf{u}}^{k+1}}{2\Delta t} + \nabla z^{k+1} = 0, \qquad \text{in } \Omega_f, \qquad (40)$$

$$\mathrm{div}\mathbf{u}^{k+1} = 0, \qquad \text{in } \Omega_f, \qquad (41)$$

$$\mathbf{u}^{k+1}\cdot\mathbf{n}|_{\partial\Omega_f\setminus\Gamma} = 0, \text{and } z^{k+1}|_\Gamma = 0. \qquad (42)$$

Furthermore, we update $p^{k+1} \in M_f$ and $\mathbf{u}^{k+1} \in \mathbf{X}_f$ by:

$$\begin{aligned}
p^{k+1} &= p^k + z^{k+1} - \chi\mu\mathrm{div}\tilde{\mathbf{u}}^{k+1},\\
\mathbf{u}^{k+1} &= \tilde{\mathbf{u}}^{k+1} - \frac{2\Delta t}{3}\nabla z^{k+1}, \qquad (43)
\end{aligned}$$

where the positive constant $0 < \chi$ is a given parameter before the computation phase begins.

Meanwhile, the following result follows from the basic analysis of BDF2 to discretize the time derivative

Lemma 4.5. *It also holds that*

$$\begin{aligned}
&3\|\delta\mathbf{u}^{k+1}\|_0^2+\frac{4}{3}\Delta t^2\|\nabla z^{k+1}\|_0^2\\
&+2\chi\mu\Delta t\left(\|\mathrm{div}\tilde{\mathbf{u}}^{k+1}\|_0^2-\|\mathrm{div}\tilde{\mathbf{u}}^{k}\|_0^2\right)+4\Delta tb\left(\delta\tilde{\mathbf{u}}^{k+1},\delta p^k\right)\\
=&3\|\delta\tilde{\mathbf{u}}^{k+1}\|_0^2+\frac{4}{3}\Delta t^2\|\nabla z^{k}\|_0^2+2\chi\mu\Delta t\|\mathrm{div}\delta\tilde{\mathbf{u}}^{k+1}\|_0^2.
\end{aligned}\tag{44}$$

Similar to the stability of BE, we first obtain the following unconditional stability for the transient NSD equations.

Theorem 4.6. *(***Unconditional stability***)Let $T>0$ be any fixed time. Then, the scheme* (39)-(43) *is unconditionally stable on* $(0,T]$.

Proof. Taking the operator δ on system (39) and substituting the test function $\vec{\mathbf{v}}=4\Delta t\delta\tilde{\vec{\mathbf{u}}}^{k+1}$ to obtain the following control of the time increments of the errors

$$\begin{aligned}
&2\left\langle\left\langle\delta\tilde{\vec{\mathbf{u}}}^{k+1},3\delta\tilde{\vec{\mathbf{u}}}^{k+1}-4\delta\vec{\mathbf{u}}^{k}+\delta\vec{\mathbf{u}}^{k-1}\right\rangle\right\rangle+4\Delta ta\left(\delta\tilde{\vec{\mathbf{u}}}^{k+1},\delta\tilde{\vec{\mathbf{u}}}^{k+1}\right)\\
&-4\Delta tb\left(\delta\tilde{\mathbf{u}}^{k+1},\delta p^k\right)+4\Delta ta_\Gamma\left(\delta\sigma\vec{\mathbf{u}}^{k},\delta\tilde{\vec{\mathbf{u}}}^{k+1}\right)\\
&+4\Delta tC\left(\delta\sigma\mathbf{u}^{k},\tilde{\mathbf{u}}^{k+1},\delta\tilde{\mathbf{u}}^{k+1}\right)-4\Delta tC\left(\sigma\mathbf{u}^{k-1},\delta\tilde{\mathbf{u}}^{k+1},\delta\tilde{\mathbf{u}}^{k+1}\right)=0.
\end{aligned}\tag{45}$$

Using the identity

$$\begin{aligned}
&2\left(\tilde{a}^{k+1},3\tilde{a}^{k+1}-4a^k+a^{k-1}\right)\\
=&3\left(|\tilde{a}^{k+1}|^2-|a^{k+1}|^2+|\tilde{a}^{k+1}-a^{k+1}|^2\right)+\left(|a^{k+1}|^2-|a^k|^2\right)\\
&+\left(|\sigma a^{k+1}|^2-|\sigma a^k|^2\right)+|\delta^2a^{k+1}|^2+2\left(\tilde{a}^{k+1}-a^{k+1},3a^{k+1}-4a^k+a^{k-1}\right),
\end{aligned}$$

setting $a^k=\delta\vec{u}^k$ and recalling the following result in [66, 72]

$$\left(\delta\mathbf{u}^{k+1}-\delta\tilde{\mathbf{u}}^{k+1},3\delta\mathbf{u}^{k+1}-4\delta\mathbf{u}^{k}+\delta\mathbf{u}^{k-1}\right)=0\tag{46}$$

yields

$$\begin{aligned}
&3\left(\|\delta\tilde{\vec{\mathbf{u}}}^{k+1}\|_0^2-\|\delta\vec{\mathbf{u}}^{k+1}\|_0^2+\|\delta\tilde{\vec{\mathbf{u}}}^{k+1}-\delta\vec{\mathbf{u}}^{k+1}\|_0^2\right)\\
&+\left(\|\delta\vec{\mathbf{u}}^{k+1}\|_0^2-\|\delta\vec{\mathbf{u}}^{k}\|_0^2\right)+\left(\|\sigma\vec{\mathbf{u}}^{k+1}\|_0^2-\|\sigma\vec{\mathbf{u}}^{k}\|_0^2\right)+\|\delta^2\vec{\mathbf{u}}^{k+1}\|_0^2\\
&+4C_a\Delta t\|\nabla\delta\tilde{\vec{\mathbf{u}}}^{k+1}\|_0^2-4\Delta tb\left(\delta\tilde{\vec{\mathbf{u}}}^{k+1},\delta p^k\right)\\
=&-4\Delta ta_\Gamma\left(\delta\sigma\vec{\mathbf{u}}^{k},\delta\tilde{\vec{\mathbf{u}}}^{k+1}\right).
\end{aligned}\tag{47}$$

Similarly, using the Young inequality

$$a^{1/2}b^{1/2}c\le\frac{\epsilon}{8}a^2+\frac{1}{2\epsilon^3}b^2+\frac{\epsilon}{2}c^2,\forall\epsilon>0,\tag{48}$$

we can obtain

$$\begin{aligned}
&a_\Gamma\left(\delta\sigma\vec{\mathbf{u}}^{k},\delta\tilde{\vec{\mathbf{u}}}^{k+1}\right)=a_\Gamma\left(\sigma\delta\vec{\mathbf{u}}^{k},\delta\tilde{\vec{\mathbf{u}}}^{k+1}\right)\\
\le&C_{ct}\|\sigma\delta\vec{\mathbf{u}}^{k}\|_\Gamma\|\delta\tilde{\vec{\mathbf{u}}}^{k+1}\|_\Gamma\\
\le&C_{ct}C_{tr}^2\|\sigma\delta\vec{\mathbf{u}}^{k}\|_0^{1/2}\|\nabla\sigma\delta\vec{\mathbf{u}}^{k}\|_0^{1/2}\|\nabla\delta\tilde{\vec{\mathbf{u}}}^{k+1}\|_0\\
\le&C_{ct}C_{tr}^2\|\sigma\delta\vec{\mathbf{u}}^{k}\|_0^{1/2}\left(\sqrt{2}\|\nabla\delta\vec{\mathbf{u}}^{k}\|_0^{1/2}+\|\nabla\delta\vec{\mathbf{u}}^{k-1}\|_0^{1/2}\right)\|\nabla\delta\tilde{\vec{\mathbf{u}}}^{k+1}\|_0\\
=&C_{ct}C_{tr}^2\left(I_1+I_2\right).
\end{aligned}$$

Noting that

$$\sigma\delta\vec{\mathbf{u}}^k = \delta\vec{\mathbf{u}}^k + \delta^2\vec{\mathbf{u}}^k,$$

and

$$\begin{aligned} I_1 \leq & \frac{\epsilon}{2}\|\nabla\delta\tilde{\vec{\mathbf{u}}}^{k+1}\|_0^2 + \frac{\epsilon}{2}\|\nabla\delta\vec{\mathbf{u}}^k\|_0^2 + \frac{1}{2\epsilon^3}\left(\|\delta\vec{\mathbf{u}}^k\|_0^2 + \|\delta^2\vec{\mathbf{u}}^k\|_0^2\right), \\ I_2 \leq & \frac{\epsilon}{2}\|\nabla\delta\tilde{\vec{\mathbf{u}}}^{k+1}\|_0^2 + \frac{\epsilon}{8}\|\nabla\delta\vec{\mathbf{u}}^{k-1}\|_0^2 + \frac{1}{2\epsilon^3}\left(\|\delta\vec{\mathbf{u}}^k\|_0^2 + \|\delta^2\vec{\mathbf{u}}^k\|_0^2\right), \end{aligned}$$

yields

$$\begin{aligned} a_\Gamma\left(\delta\sigma\vec{\mathbf{u}}^k, \delta\tilde{\vec{\mathbf{u}}}^{k+1}\right) \leq & C_{ct}C_{tr}^2\left(\epsilon\|\nabla\delta\tilde{\vec{\mathbf{u}}}^{k+1}\|_0^2 + \frac{\epsilon}{2}\|\nabla\delta\vec{\mathbf{u}}^k\|_0^2\right. \\ & \left. + \frac{\epsilon}{8}\|\nabla\delta\vec{\mathbf{u}}^{k-1}\|_0^2 + \frac{1}{\epsilon^3}\left(\|\delta\vec{\mathbf{u}}^k\|_0^2 + \|\delta^2\vec{\mathbf{u}}^k\|_0^2\right)\right). \end{aligned} \tag{49}$$

Also, setting $\epsilon = \frac{C_a}{8C_{tr}^2C_{ct}}$ gives

$$\begin{aligned} 4\Delta t a_\Gamma\left(\delta\sigma\vec{\mathbf{u}}^k, \delta\tilde{\vec{\mathbf{u}}}^{k+1}\right) \leq & \frac{C_a\Delta t}{2}\|\nabla\delta\tilde{\vec{\mathbf{u}}}^{k+1}\|_0^2 + \frac{C_a\Delta t}{4}\|\nabla\delta\vec{\mathbf{u}}^k\|_0^2 \\ & + \frac{C_a\Delta t}{16}\|\nabla\delta\vec{\mathbf{u}}^{k-1}\|_0^2 + 16\alpha\Delta t\left(\|\delta\vec{\mathbf{u}}^k\|_0^2 + \|\delta^2\vec{\mathbf{u}}^k\|_0^2\right). \end{aligned} \tag{50}$$

Choosing $\chi < C_a/4d\mu$, and using

$$\|\mathrm{div}\delta\tilde{\mathbf{u}}^{k+1}\|_0 \leq \sqrt{d}\|\nabla\delta\tilde{\mathbf{u}}^{k+1}\|_0, \tag{51}$$

we have

$$2\chi\mu\|\mathrm{div}\delta\tilde{\mathbf{u}}^{k+1}\|_0^2 \leq \frac{C_a}{2}\|\nabla\delta\tilde{\mathbf{u}}^{k+1}\|_0^2 \leq \frac{C_a}{2}\|\nabla\delta\tilde{\vec{\mathbf{u}}}^{k+1}\|_0^2. \tag{52}$$

Moreover,

$$\begin{aligned} C\left(\delta\sigma\mathbf{u}^k, \tilde{\mathbf{u}}^{k+1}, \delta\tilde{\mathbf{u}}^{k+1}\right) \leq & C_0\|\nabla\delta\sigma\mathbf{u}^k\|_0\|\nabla\tilde{\mathbf{u}}^{k+1}\|_0\|\nabla\delta\tilde{\mathbf{u}}^{k+1}\|_0 \\ \leq & C_0\left(2\|\nabla\delta\mathbf{u}^k\|_0 + \|\nabla\delta\mathbf{u}^{k-1}\|_0\right)\|\nabla\tilde{\mathbf{u}}^{k+1}\|_0\|\nabla\delta\tilde{\mathbf{u}}^{k+1}\|_0 \\ \leq & \frac{C_0}{8}\left(2\|\nabla\delta\mathbf{u}^k\|_0 + \|\nabla\delta\mathbf{u}^{k-1}\|_0\right)\|\nabla\delta\tilde{\mathbf{u}}^{k+1}\|_0 \\ \leq & \frac{C_a}{8}\|\nabla\delta\tilde{\mathbf{u}}^{k+1}\|_0^2 + \frac{C_a}{4}\|\nabla\delta\mathbf{u}^k\|_0^2 + \frac{C_a}{16}\|\nabla\delta\mathbf{u}^{k-1}\|_0^2. \end{aligned} \tag{53}$$

Using (44), observing that the bilinear form $4\Delta t b\left(\delta\tilde{\mathbf{u}}^{k+1}, \delta p^k\right)$ and $2\Delta t\chi\|\mathrm{div}\delta\tilde{\mathbf{u}}^{k+1}\|_0^2$ are absorbed, the bounds (53) of the trilinear term, and adding the term $\frac{C_a\Delta t}{8}\|\nabla\delta\vec{\mathbf{u}}^k\|_0^2$ for both side of the inequality yields

$$\begin{aligned} & 3\left(\|\delta\tilde{\vec{\mathbf{u}}}^{k+1}\|_0^2 - \|\delta\vec{\mathbf{u}}^{k+1}\|_0^2 + \|\delta\tilde{\vec{\mathbf{u}}}^{k+1} - \delta\vec{\mathbf{u}}^{k+1}\|_0^2\right) \\ & + \left(\|\delta\vec{\mathbf{u}}^{k+1}\|_0^2 - \|\delta\vec{\mathbf{u}}^k\|_0^2\right) + \left(\|\sigma\vec{\mathbf{u}}^{k+1}\|_0^2 - \|\sigma\vec{\mathbf{u}}^k\|_0^2\right) \\ & + \|\delta^2\vec{\mathbf{u}}^{k+1}\|_0^2 + 3\|\delta\mathbf{u}^{k+1}\|_0^2 + \frac{4}{3}\Delta t^2\|\nabla z^{k+1}\|_0^2 + 2\chi\mu\Delta t\|\mathrm{div}\tilde{\mathbf{u}}^{k+1}\|_0^2 \\ & + \frac{5C_a\Delta t}{2}\|\nabla\delta\tilde{\vec{\mathbf{u}}}^{k+1}\|_0^2 + \frac{C_a\Delta t}{8}\|\nabla\delta\vec{\mathbf{u}}^k\|_0^2 \\ \leq & 3\|\delta\tilde{\mathbf{u}}^{k+1}\|_0^2 + \frac{4}{3}\Delta t^2\|\nabla z^k\|_0^2 + 2\chi\mu\Delta t\|\mathrm{div}\tilde{\mathbf{u}}^k\|_0^2 \\ & + \frac{5C_a\Delta t}{8}\|\nabla\delta\vec{\mathbf{u}}^k\|_0^2 + \frac{C_a\Delta t}{8}\|\nabla\delta\vec{\mathbf{u}}^{k-1}\|_0^2 \\ & + 16\alpha\Delta t\left(\|\delta\vec{\mathbf{u}}^k\|_0^2 + \|\delta^2\vec{\mathbf{u}}^k\|_0^2\right). \end{aligned} \tag{54}$$

Then, using a simple derivation, discarding the form $3\|\delta\tilde{\vec{\mathbf{u}}}^{k+1}-\delta\vec{\mathbf{u}}^{k+1}\|_0^2$, we have

$$\begin{aligned}
&\|\delta\vec{\mathbf{u}}^{k+1}\|_0^2+\|\sigma\vec{\mathbf{u}}^{k+1}\|_0^2+\frac{4}{3}\Delta t^2\|\nabla z^{k+1}\|_0^2+2\chi\mu\Delta t\|\mathrm{div}\tilde{\mathbf{u}}^{k+1}\|_0^2\\
&+C_a\Delta t\|\nabla\delta\tilde{\vec{\mathbf{u}}}^{k+1}\|_0^2+\frac{C_a\Delta t}{8}\|\nabla\delta\vec{\mathbf{u}}^{k}\|_0^2+\|\delta^2\vec{\mathbf{u}}^{k+1}\|_0^2\\
\le&\|\delta\vec{\mathbf{u}}^{k}\|_0^2+\|\sigma\vec{\mathbf{u}}^{k}\|_0^2+\frac{4}{3}\Delta t^2\|\nabla z^{k}\|_0^2+2\chi\mu\Delta t\|\mathrm{div}\tilde{\mathbf{u}}^{k}\|_0^2+C_a\Delta t\|\nabla\delta\vec{\mathbf{u}}^{k}\|_0^2\\
&+\frac{C_a\Delta t}{8}\|\nabla\delta\vec{\mathbf{u}}^{k-1}\|_0^2+16\alpha\Delta t\left(\|\delta\vec{\mathbf{u}}^{k}\|_0^2+\|\delta^2\vec{\mathbf{u}}^{k}\|_0^2\right)
\end{aligned}$$

which implies

$$\begin{aligned}
&\|\delta\vec{\mathbf{u}}^{k+1}\|_0^2+\|\sigma\vec{\mathbf{u}}^{k+1}\|_0^2+\frac{4}{3}\Delta t^2\|\nabla z^{k+1}\|_0^2+2\chi\mu\Delta t\|\mathrm{div}\tilde{\mathbf{u}}^{k+1}\|_0^2\\
&+C_a\Delta t\|\nabla\delta\tilde{\vec{\mathbf{u}}}^{k+1}\|_0^2+\frac{C_a\Delta t}{8}\|\nabla\delta\vec{\mathbf{u}}^{k}\|_0^2+\|\delta^2\vec{\mathbf{u}}^{k+1}\|_0^2\\
\le&(1+16\alpha\Delta t)\|\delta\vec{\mathbf{u}}^{k}\|_0^2+\|\sigma\vec{\mathbf{u}}^{k}\|_0^2+\frac{4}{3}\Delta t^2\|\nabla z^{k}\|_0^2+2\chi\mu\Delta t\|\mathrm{div}\tilde{\mathbf{u}}^{k}\|_0^2\\
&+C_a\Delta t\|\nabla\delta\vec{\mathbf{u}}^{k}\|_0^2+\frac{C_a\Delta t}{8}\|\nabla\delta\vec{\mathbf{u}}^{k-1}\|_0^2+\|\delta^2\vec{\mathbf{u}}^{k}\|_0^2.
\end{aligned}$$

Thus, the proof is proved. □

To prove the long time stability of the BDF2 rotational pressure-correction method, we utilize the G-stability framework as in [46]. For the BDF2, the positive definite G-matrixs

$$\begin{pmatrix}\frac{1}{2} & -1\\ -1 & \frac{5}{2}\end{pmatrix}$$

and the associated norms can be obtained as

$$|\vec{\mathbf{U}}|_G^2=(\vec{\mathbf{U}},G\vec{\mathbf{U}}),\ \vec{\mathbf{U}}\in[L^2(\Omega)]^d.$$

Also, we apply the G matrix to functions belonging to $\overline{\mathbf{X}}$: for any $\vec{\mathbf{U}}\in\overline{\mathbf{X}}^2$, define $|\vec{\mathbf{u}}|_G^2=(\vec{\mathbf{u}},G\vec{\mathbf{u}})$. Then, for any $\vec{\mathbf{u}}^i\in\overline{\mathbf{X}}, i=k+1,k,k-1$ [73] of the BDF2,

$$\left\langle\left\langle D_t^2\tilde{\vec{\mathbf{u}}}^{k+1},\tilde{\vec{\mathbf{u}}}^{k+1}\right\rangle\right\rangle=\frac{1}{2}(|\tilde{\vec{\mathbf{U}}}^{k+1}|_G^2-|\vec{\mathbf{U}}^{k}|_G^2)+\frac{1}{4}\|\delta^2\tilde{\vec{\mathbf{u}}}^{k+1}\|_S^2 \tag{55}$$

where $\tilde{\vec{\mathbf{U}}}^{k+1}=[\tilde{\vec{\mathbf{u}}}^{k+1},\vec{\mathbf{u}}^{k}]^T$ and $\vec{\mathbf{U}}^{k}=[\vec{\mathbf{u}}^{k},\vec{\mathbf{u}}^{k-1}]^T$.

Moreover, the G-norm and L^2-norm, and $\|\cdot\|_S$ and $\|\cdot\|_0$ are equivalent in the sense that $|\vec{\mathbf{U}}|_G\sim\|\vec{\mathbf{U}}\|_0$ and $\|\delta^2\tilde{\vec{\mathbf{u}}}^{k+1}\|_S\sim\|\delta^2\tilde{\vec{\mathbf{u}}}^{k+1}\|_0$ without regards to the positive constants.

Theorem 4.7. *(**Long time stability**) Assume that the time-step restriction* $8\alpha\Delta t<1$ *is satisfied. Then, the solution to* (39)-(43) *is uniformly bounded for all time.*

Proof. Taking the operator δ on system (39), substituting the test function $\vec{\mathbf{v}}=4\Delta t\delta\tilde{\vec{\mathbf{u}}}^{k+1}$ and applying the identity $(a-b,a)=a^2-b^2+(a-b)^2$ to obtain the following control of the time increments of the errors

$$\begin{aligned}
&2|\delta\tilde{\vec{\mathbf{U}}}^{k+1}|_G^2-2|\delta\vec{\mathbf{U}}^{k}|_G^2+\|\delta^3\tilde{\vec{\mathbf{u}}}^{k+1}\|_S^2+4C_a\Delta t\|\nabla\delta\tilde{\vec{\mathbf{u}}}^{k+1}\|_0^2\\
&-4\Delta tb\left(\delta\tilde{\mathbf{u}}^{k+1},\delta p^{k}\right)+4\Delta ta_\Gamma\left(\delta\vec{\mathbf{u}}^{k},\delta\tilde{\vec{\mathbf{u}}}^{k+1}\right)\\
&+4\Delta tC\left(\delta\sigma\mathbf{u}^{k},\tilde{\mathbf{u}}^{k+1},\delta\tilde{\mathbf{u}}^{k+1}\right)-4\Delta tC\left(\sigma\mathbf{u}^{k-1},\delta\tilde{\mathbf{u}}^{k+1},\delta\tilde{\mathbf{u}}^{k+1}\right)=0.
\end{aligned} \tag{56}$$

Choosing $\chi < C_a/16d\mu$, and the estimate

$$\|\mathrm{div}\delta\tilde{\mathbf{u}}^{k+1}\|_0 \le \sqrt{d}\|\nabla\delta\tilde{\mathbf{u}}^{k+1}\|_0, \tag{57}$$

we have

$$2\chi\mu\|\mathrm{div}\delta\tilde{\mathbf{u}}^{k+1}\|_0^2 \le \frac{C_a}{8}\|\nabla\delta\tilde{\mathbf{u}}^{k+1}\|_0^2 \le \frac{C_a}{8}\|\nabla\delta\tilde{\vec{\mathbf{u}}}^{k+1}\|_0^2. \tag{58}$$

Recalling the equivalence between $\|\cdot\|_0$ and $\|\cdot\|_S$, using the Young inequality $a^{1/2}b^{1/2}c \le \frac{a^2}{8\epsilon^3} + \frac{\epsilon b^2}{2} + \frac{\epsilon a^2}{2}$ with $\epsilon = \frac{C_a}{8C_{ct}C_{tr}^2}$, and noticing

$$a_\Gamma\left(\delta\vec{\mathbf{u}}^{k+1}, \delta\vec{\mathbf{u}}^{k+1}\right) = 0,$$

yields

$$\begin{aligned}
&4\Delta t a_\Gamma\left(\delta\sigma\vec{\mathbf{u}}^k, \delta\tilde{\vec{\mathbf{u}}}^{k+1}\right)\\
=&4\Delta t a_\Gamma\left(\sigma\delta\vec{\mathbf{u}}^k - \delta\tilde{\vec{\mathbf{u}}}^{k+1}, \delta\tilde{\vec{\mathbf{u}}}^{k+1}\right)\\
=&-4\Delta t a_\Gamma\left(\delta^3\tilde{\vec{\mathbf{u}}}^{k+1}, \delta\tilde{\vec{\mathbf{u}}}^{k+1}\right)\\
\le&4C_{ct}\Delta t\|\delta^3\tilde{\vec{\mathbf{u}}}^{k+1}\|_\Gamma\|\delta\tilde{\vec{\mathbf{u}}}^{k+1}\|_\Gamma\\
\le&4C_{ct}C_{tr}^2\Delta t\|\delta^3\tilde{\vec{\mathbf{u}}}^{k+1}\|_0^{1/2}\|\nabla\delta^3\vec{\mathbf{u}}^{k+1}\|_0^{1/2}\|\nabla\delta\tilde{\vec{\mathbf{u}}}^{k+1}\|_0\\
\le&4C_{ct}C_{tr}^2\Delta t\|\delta^3\tilde{\vec{\mathbf{u}}}^{k+1}\|_S^{1/2}\left(\|\nabla\delta\tilde{\vec{\mathbf{u}}}^{k+1}\|_0^{1/2}\right.\\
&\left.+\sqrt{2}\|\nabla\delta\vec{\mathbf{u}}^k\|_0^{1/2} + \|\nabla\delta\vec{\mathbf{u}}^{k-1}\|_0^{1/2}\right)\|\nabla\delta\tilde{\vec{\mathbf{u}}}^{k+1}\|_0\\
\le&C_a\Delta t\|\nabla\delta\tilde{\vec{\mathbf{u}}}^{k+1}\|_0^2 + C_a\Delta t\|\nabla\delta\vec{\mathbf{u}}^k\|_0^2 + \frac{C_a\Delta t}{4}\|\nabla\delta\vec{\mathbf{u}}^{k-1}\|_0^2 + 8\alpha\Delta t\|\delta^3\tilde{\vec{\mathbf{u}}}^{k+1}\|_S^2.
\end{aligned}$$

Using (58), the bounds (53) of the trilinear term, and noting that the bilinear term $2\Delta t b\left(\delta\tilde{\mathbf{u}}^{k+1}, \delta p^k\right)$ and $\Delta t\chi\|\mathrm{div}\delta\tilde{\mathbf{u}}^{k+1}\|_0^2$ are absorbed, yields

$$\begin{aligned}
&2|\delta\tilde{\vec{\mathbf{U}}}^{k+1}|_G^2 + (1-8\alpha\Delta t)\|\delta^3\tilde{\vec{\mathbf{u}}}^{k+1}\|_S^2 + \frac{13C_a\Delta t}{8}\|\nabla\delta\tilde{\vec{\mathbf{u}}}^{k+1}\|_0^2\\
&+3\|\delta\mathbf{u}^{k+1}\|_0^2 + \frac{4\Delta t^2}{3}\|\nabla z^{k+1}\|_0^2 + 2\chi\mu\Delta t\|\mathrm{div}\tilde{\mathbf{u}}^{k+1}\|_0^2\\
\le&2|\delta\vec{\mathbf{U}}^k|_G^2 + \frac{5C_a}{4}\Delta t\|\nabla\delta\vec{\mathbf{u}}^k\|_0^2 + \frac{5C_a\Delta t}{16}\|\nabla\delta\vec{\mathbf{u}}^{k-1}\|_0^2\\
&+3\|\delta\tilde{\mathbf{u}}^{k+1}\|_0^2 + \frac{4\Delta t^2}{3}\|\nabla z^k\|_0^2 + 2\chi\mu\Delta t\|\mathrm{div}\tilde{\mathbf{u}}^k\|_0^2.
\end{aligned} \tag{59}$$

Setting $8\alpha\Delta t < 1$, discarding $\|\delta^3\tilde{\vec{\mathbf{u}}}^{k+1}\|_S^2$, and adding $\frac{5C_a\Delta t}{16}\|\nabla\delta\vec{\mathbf{u}}^k\|_0^2$ to both side of the above inequality, implies

$$\begin{aligned}
&2|\delta\tilde{\vec{\mathbf{U}}}^{k+1}|_G^2 + \frac{13C_a\Delta t}{8}\|\nabla\delta\tilde{\vec{\mathbf{u}}}^{k+1}\|_0^2 + \frac{5C_a\Delta t}{16}\|\nabla\delta\vec{\mathbf{u}}^k\|_0^2\\
&+3\|\delta\mathbf{u}^{k+1}\|_0^2 + \frac{4\Delta t^2}{3}\|\nabla z^{k+1}\|_0^2 + 2\chi\mu\Delta t\|\mathrm{div}\tilde{\mathbf{u}}^{k+1}\|_0^2\\
\le&2|\delta\vec{\mathbf{U}}^k|_G^2 + \frac{25C_a\Delta t}{16}\|\nabla\delta\vec{\mathbf{u}}^k\|_0^2 + \frac{5C_a\Delta t}{16}\|\nabla\delta\vec{\mathbf{u}}^{k-1}\|_0^2\\
&+3\|\delta\tilde{\mathbf{u}}^{k+1}\|_0^2 + \frac{4\Delta t^2}{3}\|\nabla z^k\|_0^2 + 2\chi\mu\Delta t\|\mathrm{div}\tilde{\mathbf{u}}^k\|_0^2.
\end{aligned} \tag{60}$$

Hence, the theorem is proved. □

5. Fully discretized numerical schemes

In this section, we aim to provide the first order and second order fully discretized rotational pressure-correction method for the coupled NSD system.

We assume that the subdivisions of Ω_f and Ω_p are $\mathcal{T}_f$ and $\mathcal{T}_p$, respectively. The elements of each of two subdivisions exactly match along Γ [74, 75]. Based on two subdivisions $\mathcal{T}_f$ and $\mathcal{T}_p$, the finite element spaces $\mathbf{X}_f^h \subset \mathbf{X}_f$, $X_p^h \subset X_p$ and $M_f^h \subset M_f$ with the mesh scale h can be defined.

5.1. The fully discrete BE.

The standard finite element approximation of (1)-(10) are defined by using the following fully discrete BE rotational pressure-correction method: Given $\Delta t > 0$, $\vec{\mathbf{f}} \in [H^{-1}(\Omega_i)]^d$, find $\tilde{\vec{\mathbf{u}}}_h^{k+1} \equiv (\tilde{\mathbf{u}}_h^{k+1}, \phi_h^{k+1}) \in \overline{\mathbf{X}}^h$ such that

$$\left\langle\left\langle \frac{D_1^t \tilde{\vec{\mathbf{u}}}_h^{k+1}}{\Delta t}, \vec{\mathbf{v}}_h \right\rangle\right\rangle + a\left(\tilde{\vec{\mathbf{u}}}_h^{k+1}, \vec{\mathbf{v}}_h\right) - b\left(\mathbf{v}_h, p_h^k\right) + a_\Gamma\left(\vec{\mathbf{u}}_h^k, \vec{\mathbf{v}}_h\right) + C\left(\mathbf{u}_h^k, \tilde{\mathbf{u}}_h^{k+1}, \mathbf{v}_h\right)$$
$$= \left(\vec{\mathbf{f}}_h^{k+1}, \vec{\mathbf{v}}_h\right), \quad \forall \vec{\mathbf{v}} \in \overline{\mathbf{X}}^h. \tag{61}$$

Find $\left(\mathbf{u}_h^{k+1}, z_h^{k+1}\right) \in \mathbf{X}_f^h \times M_f^h$ such that $\forall\, (\mathbf{v}_h, q_h) \in \mathbf{X}_f^h \times M_f^h$

$$\left(\frac{\mathbf{u}_h^{k+1} - \tilde{\mathbf{u}}_h^{k+1}}{\Delta t}, \nabla q_h\right) + \left(\nabla z_h^{k+1}, \nabla q_h\right) = 0, \qquad \text{in } \Omega_f, \tag{62}$$

$$b\left(\mathbf{u}_h^{k+1}, q_h\right) = 0, \qquad \text{in } \Omega_f, \tag{63}$$

$$\mathbf{u}_h^{k+1} \cdot \mathbf{n}|_{\partial\Omega_f \setminus \Gamma} = 0, \text{and } z_h^{k+1}|_\Gamma = 0. \tag{64}$$

Furthermore, update the pressure by

$$p_h^{k+1} = p_h^k + z_h^{k+1} - \chi\mu \mathrm{div}\tilde{\mathbf{u}}_h^{k+1}. \tag{65}$$

Here, $D_1^t \tilde{\vec{\mathbf{u}}}_h^{k+1} = \tilde{\vec{\mathbf{u}}}_h^{k+1} - \vec{\mathbf{u}}_h^k$ denotes the difference operator.

5.2. The fully discrete BDF2.

For the numerical treatment of time derivative term, we use the fully discrete BDF2. The standard finite element approximation of (1)-(10) are defined using the following rotational pressure-correction method: Given $\Delta t > 0$, $\vec{\mathbf{f}} \in [H^{-1}(\Omega_i)]^d$, find $\tilde{\vec{\mathbf{u}}}_h^{k+1} \equiv \left(\tilde{\mathbf{u}}_h^{k+1}, \phi_h^{k+1}\right) \in \overline{\mathbf{X}}^h$ such that

$$\left\langle\left\langle \frac{D_2^t \tilde{\vec{\mathbf{u}}}_h^{k+1}}{2\Delta t}, \vec{\mathbf{v}}_h \right\rangle\right\rangle + a\left(\tilde{\vec{\mathbf{u}}}_h^{k+1}, \vec{\mathbf{v}}_h\right) - b\left(\mathbf{v}_h, p_h^k\right) + a_\Gamma\left(\sigma\vec{\mathbf{u}}_h^k, \vec{\mathbf{v}}_h\right) + C\left(\sigma\mathbf{u}_h^k, \tilde{\mathbf{u}}_h^{k+1}, \mathbf{v}_h\right)$$
$$= \left(\vec{\mathbf{f}}^{k+1}, \vec{\mathbf{v}}_h\right), \quad \forall \vec{\mathbf{v}}_h \in \overline{\mathbf{X}}^h. \tag{66}$$

Find $\left(\mathbf{u}_h^{k+1}, z_h^{k+1}\right) \in \mathbf{X}_f^h \times M_f^h$ such that $\forall\, (\mathbf{v}_h, q_h) \in \mathbf{X}_f^h \times M_f^h$

$$\left(\frac{3\mathbf{u}_h^{k+1} - 3\tilde{\mathbf{u}}_h^{k+1}}{2\Delta t}, \nabla q_h\right) + \left(\nabla z_h^{k+1}, \nabla q_h\right) = 0, \qquad \text{in } \Omega_f, \tag{67}$$

$$b\left(\mathbf{u}_h^{k+1}, q_h\right) = 0, \qquad \text{in } \Omega_f, \tag{68}$$

$$\mathbf{u}_h^{k+1} \cdot \mathbf{n}|_{\partial\Omega_f \setminus \Gamma} = 0, \text{and } z_h^{k+1}|_\Gamma = 0. \tag{69}$$

Furthermore, update the pressure by

$$p_h^{k+1} = p_h^k + z_h^{k+1} - \chi\mu \mathrm{div}\tilde{\mathbf{u}}_h^{k+1}. \tag{70}$$

Here, $D_2^t\tilde{\vec{\mathbf{u}}}_h^{k+1} = 3\tilde{\vec{\mathbf{u}}}_h^{k+1} - 4\vec{\mathbf{u}}_h^k + \vec{\mathbf{u}}_h^{k-1}$ denotes the second order difference operator for temporal discretization.

Remark 5.1. The quantity $(u_h^0, \phi_h^0, p_h^0) \in \mathbf{X}_f^h \times X_p^h \times M_f^h$ is set to be a suitable approximation of the initial data of the problem. Then we compute an approximation of the exact solution at time $t = \Delta t$, say $(u_h^1, \phi_h^1, p_h^1) \in \mathbf{X}_f^h \times X_p^h \times M_f^h$ by using the corresponding fully discrete BE.

Remark 5.2. Equations (62)-(64) and (67)-(69) can be computed by the following:
Find $(\mathbf{u}_h^{k+1}, z_h^{k+1}) \in \mathbf{X}_f^h \times M_f^h$ such that $\forall (\mathbf{v}_h, q_h) \in \mathbf{X}_f^h \times M_f^h$

$$(\nabla z_h^{k+1}, \nabla q_h) = -\frac{2+\theta}{2\Delta t}(\mathbf{u}_h^{k+1} - \tilde{\mathbf{u}}_h^{k+1}, q_h), \qquad \text{in } \Omega_f, \tag{71}$$

$$\mathbf{u}_h^{k+1} \cdot \mathbf{n}|_{\partial\Omega_f \setminus \Gamma} = 0 \text{ and } z_h^{k+1}|_\Gamma = 0. \tag{72}$$

For $\theta = 0$, we have the BE. We consider the case of the BDF2 where $\theta = 1$.

Remark 5.3. These two schemes are, in fact, time-dependent version domain decomposition, which has first-order or second-order accuracy without the incompressibility constraint of the incompressible Naiver-Stokes system. In particular especially, the incompressible flow is decoupled by two separate steps to obtain the velocity and pressure, respectively. Therefore, computation load is greatly reduced for the whole coupled large scale system.

6. Numerical examples

In this section, we perform several numerical tests to validate proposed rotational pressure-correction projection schemes. In the first numerical example, we present the errors between the analytical solution and approximate solution for the backward-Euler scheme `RPC-BE`, and second-order rotational pressure-correction projection backward difference formula `RPC-BDF2`, respectively by taking the exact solution of the model problem. Moreover, several numerical experiments are performed to show the flow speed, streamlines, and pressure contour by constructing a geometrical set-up with the reservoir domain and pipe flow. On the other hand, we also study the long-time stability over the long time interval to show the long-time behavior of the proposed algorithms. To discretize the NSD system, we utilize the well-known MINI elements pair $P_{1b} - P_1$ for the Navier-Stokes equations to guarantee the stability of the system. Besides, linear Lagrangian element P_1 is used to discretize the Darcy equations. Furthermore, Hood-Taylor element pair $P_2 - P_1$ is considered for the Navier-Stokes equation and quadratic elements P_2 is considered for the matrix pressure to show the performance with the higher order element of the proposed numerical methods. The code is implemented by using the software package FreeFEM++ [77]

For comparison purposes, the following error indicators will be applied to compute the absolute error between the exact solution and approximate solutions respective part of the domain Ω_f and Ω_p:

$$e_{h,\tilde{\mathbf{u}}}^k = \mathbf{u}(t^k) - \tilde{\mathbf{u}}^k,\ e_{h,\mathbf{u}}^k = \mathbf{u}(t^k) - \mathbf{u}^k,\ e_{h,p}^k = p(t^k) - p^k,\ e_{h,\phi}^k = \phi(t^k) - \phi^k.$$

In all the numerical tests, we set physical parameters $\nu, g, \alpha = 1.0$ and $z = 0$.

6.1. Approximate Accuracy.

To conduct the analytical solution test, the global domain Ω is divided into two subdomains with free fluid flow region $\Omega_f = [0,1] \times [1,2]$ and the porous media region $\Omega_p = [0,1] \times [0,1]$ which is separated by a common interface $\Gamma = (0,1) \times \{1\}$.

TABLE 1. Approximate accuracy of varying mesh scales with fixed time step size $\Delta t = 0.001$ for RPC-BE at $T = 0.5$.

$1/h$	$\|\|\nabla e^{k+1}_{h,\tilde{\mathbf{u}}}\|\|_0$	Rate	$\|\|\nabla e^{k+1}_{h,\mathbf{u}}\|\|_0$	Rate	$\|\|e^{k+1}_{h,p}\|\|_0$	Rate	$\|\|\nabla e^{k+1}_{h,\phi}\|\|_0$	Rate
4	1.29424	-	1.29274	-	0.65610	-	1.49941	-
8	0.64570	1.003	0.64454	1.003	0.21944	1.580	0.78162	0.939
16	0.32177	1.004	0.32154	1.003	0.07884	1.476	0.39529	0.983
32	0.16059	1.002	0.16075	1.000	0.03071	1.360	0.19823	0.995
64	0.08034	0.999	0.08089	0.990	0.01435	1.097	0.09920	0.998

TABLE 2. Approximate accuracy of varying mesh scales with fixed time step size $\Delta t = 0.001$ for RPC-BDF2 at $T = 0.5$.

$1/h$	$\|\|\nabla e^{k+1}_{h,\tilde{\mathbf{u}}}\|\|_0$	Rate	$\|\|\nabla e^{k+1}_{h,\mathbf{u}}\|\|_0$	Rate	$\|\|e^{k+1}_{h,p}\|\|_0$	Rate	$\|\|\nabla e^{k+1}_{h,\phi}\|\|_0$	Rate
4	1.29372	-	1.29269	-	0.65151	-	1.49947	-
8	0.64624	0.805	0.64511	1.011	0.23013	1.509	0.78165	0.940
16	0.32202	1.004	0.32172	1.004	0.08372	1.458	0.39531	0.983
32	0.16064	1.003	0.16074	1.001	0.03111	1.427	0.19824	0.996
64	0.08034	0.999	0.08075	0.993	0.01340	1.215	0.09919	0.999

The following exact solution of the model problem satisfies the interface conditions (6)-(8):

$$\vec{u} = \begin{bmatrix} \left(x^2(y-1)^2 + y\right) cos(t) \\ \left(-2/3x(y-1)^3 + 2 - \pi sin(\pi x)\right) cos(t) \end{bmatrix},$$
$$p = (2 - \pi sin(\pi x))\, sin(0.5\pi y) cos(t),$$
$$\phi = (2 - \pi sin(\pi x))\,(1 - y - cos(\pi y))\, cos(t).$$

The initial conditions, boundary conditions, and the forcing terms $\mathbf{f}$ and f follow the solution with $S = 1$.

Tables 1-2, illustrates the errors between the approximate solution and exact solutions of the RPC-BE and RPC-BDF2 respectively, with a fixed time step $\Delta t = 0.001$ and varying mesh size $h = 1/4, 1/8, 1/16, /32, 1/64$. The tables shows that, we achieve the optimal convergence order with $O(h)$ for $\tilde{\mathbf{u}}_h$, $\mathbf{u}_h$ and ϕ_h in H^1-norm and p_h in L^2-norm in space for both schemes. On the other hand, to confirm the theoretical prediction with time step size Δt, for RPC-BE, we set $h = O(\Delta t)$ for $\tilde{\mathbf{u}}_h$, $\mathbf{u}_h$ and ϕ_h in H^1-norm and p_h in L^2-norm. Besides, we consider $h = O(\Delta t^2)$ for $\tilde{\mathbf{u}}_h$, $\mathbf{u}_h$ and ϕ_h in H^1-norm and p_h in L^2-norm to check the convergence order of the algorithm RPC-BDF2. Tables 3-4 presents that first order in time for the rotational pressure-correction projection backward-Euler scheme RPC-BE and second order for rotational pressure-correction projection backward finite difference scheme RPC-BDF2, which completely agrees with the optimal predicated rates.

Furthermore, we listed the errors in Table 5 of the RPC-BES for the $P_2 - P_1 - P_2$ finite element triple with the fixed time step size $\Delta t = 0.001$, varying mesh size $h = 1/4, 1/8, 1/16, /32, 1/64$ and final time $T = 0.5$. One can clearly observe that we achieve almost second-order accuracy for $\tilde{\mathbf{u}}_h$, $\mathbf{u}_h$ and ϕ_h in H^1-norm. However, we lose approximate accuracy in the last step of the computations. In Table 5, due to the mismatch between the time step and the space step, the accuracy of the calculation results began to lose with the decrease of the space step when the time step was fixed. To improve the convergence order, we set $\Delta t = h^2$ in Table 6 and obtain the second order accuracy $O(h^2)$ for $\tilde{\mathbf{u}}_h$, $\mathbf{u}_h$ and ϕ_h in H^1-norm and p_h in L^2-norm.

Finally, the analytical solution test is carried out, and the whole region Ω is divided into two sub-regions. Free fluid flowing area $\Omega_f = [0,1] \times [0,1] \times [1,2]$ and porous media region $\Omega_f = [0,1] \times [0,1] \times [0,1]$ by public interface $\Gamma = (0,1) \times (0,1) \times \{1\}$. The following exact solutions of the model problem satisfy the interface

TABLE 3. Approximate accuracy of time step size for RPC-BE with $h = O(\Delta t)$ at $T = 0.5$.

$1/\Delta t$	$1/h = 2/\Delta t$	$\|\|\nabla e_{h,\vec{\mathbf{u}}}^{k+1}\|\|_0$	Rate	$\|\|\nabla e_{h,\mathbf{u}}^{k+1}\|\|_0$	Rate	$\|\|e_{h,p}^{k+1}\|\|_0$	Rate	$\|\|\nabla e_{h,\phi}^{k+1}\|\|_0$	Rate
4	8	0.80019	-	1.07930	-	0.45027	-	0.78341	-
8	16	0.41687	0.940	0.65730	0.715	0.25187	0.838	0.39746	0.978
16	32	0.17821	1.226	0.22255	1.562	0.07747	1.700	0.19861	1.000
32	64	0.08436	1.078	0.09428	1.238	0.03383	1.195	0.09934	0.999
64	128	0.04115	1.035	0.04439	1.086	0.01429	1.242	0.04966	1.000

TABLE 4. Approximate accuracy of time step size for RPC-BDF2 with $h = O(\Delta t^2)$ at $T = 0.5$.

$1/\Delta t$	$1/h = 16/\Delta t^2$	$\|\|\nabla e_{h,\vec{\mathbf{u}}}^{k+1}\|\|_0$	Rate	$\|\|\nabla e_{h,\mathbf{u}}^{k+1}\|\|_0$	Rate	$\|\|e_{h,p}^{k+1}\|\|_0$	Rate	$\|\|\nabla e_{h,\phi}^{k+1}\|\|_0$	Rate
8	4	1.34178	-	0.65730	-	0.51856	2.389	1.50209	-
16	16	0.34690	1.994	0.22255	1.951	0.09895	2.389	0.39534	1.925
32	64	0.09097	1.989	0.09428	1.931	0.02684	1.882	0.09920	1.994
64	256	0.02558	1.984	0.04439	1.830	0.00627	2.096	0.02483	1.998

TABLE 5. Approximate accuracy of varying mesh scales with fixed time step size $\Delta t = 0.001$ for RPC-BE at $T = 0.5$ by using $P_2 - P_1 - P_2$ finite elements.

$1/h$	$\|\|\nabla e_{h,\vec{\mathbf{u}}}^{k+1}\|\|_0$	Rate	$\|\|\nabla e_{h,\mathbf{u}}^{k+1}\|\|_0$	Rate	$\|\|e_{h,p}^{k+1}\|\|_0$	Rate	$\|\|\nabla e_{h,\phi}^{k+1}\|\|_0$	Rate
4	0.14123	-	0.14121	-	0.04647	-	0.27693	-
8	0.03550	1.991	0.03550	2.008	0.01110	2.065	0.07201	1.943
16	0.00895	1.988	0.00895	1.988	0.00302	1.875	0.01823	1.981
32	0.00233	1.936	0.00234	1.931	0.00122	1.302	0.00458	1.992
64	0.00080	1.535	0.00081	1.517	0.00091	0.421	0.00115	1.982

TABLE 6. Approximate accuracy of time step size for RPC-BE with $h = O(\Delta t^2)$ at $T = 0.5$ by using $P_2 - P_1 - P_2$ finite elements.

$1/h$	$1/\Delta t = 1/h^2$	$\|\|\nabla e_{h,\vec{\mathbf{u}}}^{k+1}\|\|_0$	Rate	$\|\|\nabla e_{h,\mathbf{u}}^{k+1}\|\|_0$	Rate	$\|\|e_{h,p}^{k+1}\|\|_0$	Rate	$\|\|\nabla e_{h,\phi}^{k+1}\|\|_0$	Rate
4	16	0.192146	-	0.198534	-	0.162541	-	0.277336	-
8	64	0.044445	2.112	0.043909	2.176	0.038446	2.079	0.072064	1.944
16	256	0.009297	2.257	0.009344	2.232	0.004698	3.023	0.018247	1.981
32	1024	0.002332	1.994	0.002335	2.000	0.001207	1.959	0.004581	1.993
64	4096	0.000573	2.023	0.000573	2.025	0.000273	2.142	0.001147	1.997

conditions (6)-(8):

$$\vec{u} = \begin{bmatrix} \left(2x\sin(xy) + y\left(x^2+y^2-8\right)\cos(xy)\right)\mathrm{e}^{-t} \\ \left(2y\sin(xy) + x\left(x^2+y^2-8\right)\cos(xy)\right)\mathrm{e}^{-t} \\ 1 + \left(\left(x^2+y^2\right)\left(x^2+y^2-8\right)\sin(xy) - 4\sin(xy) - 8xy\cos(xy)\right) z\mathrm{e}^{-t} \end{bmatrix},$$

$$p = (-16xy\cos(xy) + \left(x^2+y^2+z^2-8\right)\left(2x^2+2y^2+2z^2-1\right)\sin(xy) - 8\sin(xy)\right)\mathrm{e}^{-t},$$

$$\phi = -z - \left(x^2+y^2-8\right)\mathrm{e}^{-t}\sin(xy)\cos(z).$$

The initial conditions, boundary conditions, and the forcing terms $\mathbf{f}$ and f follow the solution with $S = 1$.

For convenience, we are defined as follows

$$\rho_{k,v} = \frac{\left\|v^{h,k} - v^{h,k/2}\right\|_0}{\left\|v^{h,k/2} - v^{h,k/4}\right\|_0},$$

where $v = \vec{u}, p, \phi$. In particular, when $\rho_{k,v} \approx 4$, the corresponding convergence order is 2. Thus, let $h = 1/10, \Delta t = 1/40, 1/80, 1/160, 1/320$ to calculate the time convergence order of model (2.1)-(2.5). It can be seen from Table 7 that for BE schemes, the optimal convergence order of $\vec{u}, p, \phi$ are $O(\Delta t)$ in L^2-norm. Meanwhile, it can be seen from Table 8 that for BDF2 schemes, the optimal convergence order of $\vec{u}, p, \phi$ are $O(\Delta t^2)$ in L^2-norm.

TABLE 7. Approximate accuracy of time step size for RPC-BE with $h = 1/10$ by using $P_2 - P_1 - P_2$ finite elements.

$1/\Delta t$	$\|\vec{u}^{h,k} - \vec{u}^{h,k/2}\|_0$	Rate	$\|p^{h,k} - p^{h,k/2}\|_0$	Rate	$\|\phi^{h,k} - \phi^{h,k/2}\|_0$	Rate
40	9.01254e-04	-	0.0747446	-	2.38021e-03	-
80	4.44203e-04	1.02071	0.0364006	1.03801	1.16908e-03	1.02571
160	2.20507e-04	1.01039	0.0179628	1.01895	5.79351e-04	1.01287
320	1.09856e-04	1.00521	0.0089227	1.00946	2.88386e-04	1.00643

TABLE 8. Approximate accuracy of time step size for RPC-BDF2 with $h = 1/10, \Delta t = 1/40, 1/80, 1/160, 1/320$ at $T = 0.5$ by using $P_2 - P_1 - P_2$ finite elements.

$1/\Delta t$	$\|\vec{u}^{h,k} - \vec{u}^{h,k/2}\|_0$	Rate	$\|p^{h,k} - p^{h,k/2}\|_0$	Rate	$\|\phi^{h,k} - \phi^{h,k/2}\|_0$	Rate
40	9.80649e-06	-	0.000555998	-	2.32204e-05	-
80	2.41939e-06	2.01909	0.000137021	2.02069	5.72404e-06	2.02029
160	6.00865e-07	2.00953	3.40102e-05	2.01036	1.42099e-06	2.01014
320	1.49721e-07	2.00476	8.47198e-06	2.00519	3.54003e-07	2.00507

6.2. Vertical Production Wellbore Attached with a Reservoir.

In this numerical experiments, we construct a simplified computational domain with the reservoir flow, which represents the porous media region Ω_p governed by the Darcy's law and the vertical production wellbore Ω_f describes the conduit region modeled by the Navier-Stokes equations. Several numerical tests are conducted to show the streamlines, magnitudes, and pressure contour by applying the proposed RPC-BE and RPC-BDF2, respectively. On the other hand, we compare the computational results of the proposed methods with the traditional backward-Euler scheme (T-BE).

Figure 2 presents the computational domain consists of a porous medium Ω_p and pipe region Ω_f. On the interface $\Gamma = \Gamma_1 \cup \Gamma_2 \cup \Gamma_3$ between the porous medium region and pipe region, we utilize the corresponding interface conditions (6)-(8). No-slip boundary condition $\mathbf{u} = 0$ is considered on the boundaries $\partial\Omega_f \backslash \Gamma$ of the vertical production wellbore. Homogeneous Neumann boundary condition $(-p\mathbb{I} + 2\mu\mathbb{D}(\mathbf{u})) \cdot \mathbf{n}_f = 0$ is imposed on the top of the vertical well for the free outflow. The porous media flow velocity is computed by setting $\vec{u}_p = -\mathbb{K}\nabla\phi$. On the boundaries of the porous medium $\partial\Omega_p \backslash \Gamma$, we use constant inflow boundary condition by setting $\phi = 10^2$.

We set the parameters value in the following way $\mathbb{K} = k\mathbb{I}$, $(k = 0.1)$, and $S = 10^{-5}$. The body fores $\mathbf{f}$ and f are taken as 0. The Navier-Stokes pressure $p = 0$ on all the boundaries of $\partial\Omega_f$. The mesh size, time step size and final time are assumed as $h_{max} = 0.025, \Delta t = 0.001$ and $T = 5.0$, respectively.

Figure 3, illustrate the flow speed and streamlines around a vertical production wellbore attached with a reservoir for the T-BE, RPC-BE and RPC-BDF2, schemes with final time $T = 5.0$ by using $P_{1b} - P_1 - P_1$ finite element triple. The basic properties of fluid and mass transfer in natural fractured reservoirs indicate that the high pressure in the porous media region pushes the fluid to the production wellbore. As expected, flowlines show flow from the reservoir to the vertical production wellbore. In addition, red indicates the highest flow rate in the wellbore and blue indicates the lowest flow rate in the reservoir. On the other hand, Figure 4 shows a higher pressure in the porous media area, which gradually decreases towards the wellbore.

Figure 5, presents the magnitudes and streamlines for the proposed numerical methods T-BE, RPC-BE and RPC-BDF2, respectively by using $P_2 - P_1 - P_2$ finite element triples. Obviously, we can see that the left and right figures are similar to Figure 3.

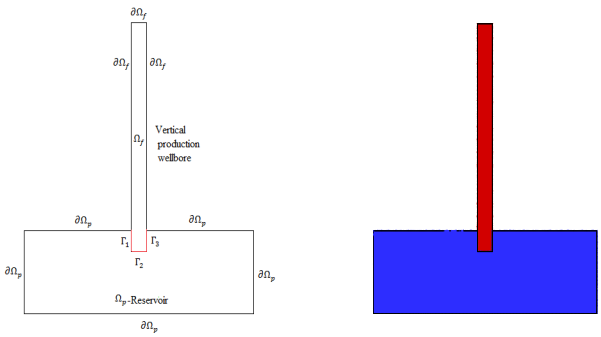

FIGURE 2. Left: the computational domain with free flow region Ω_f and porous media flow region Ω_p; Right: the illustration of the computational mesh.

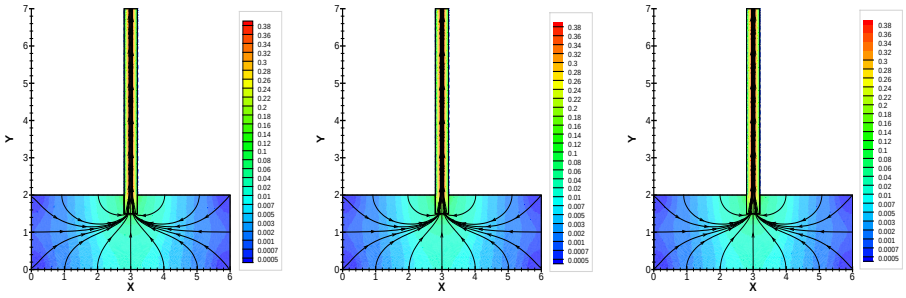

FIGURE 3. The flow speed and streamlines around a vertical production wellbore attatched with a reservoir for $\phi = 10^2$ on $\partial\Omega_p \setminus \Gamma$, $\Delta t = 0.001$ and $T = 5.0$. Left: `T-BE`; Middle: `RPC-BE`; Right: `RPC-BDF2`.

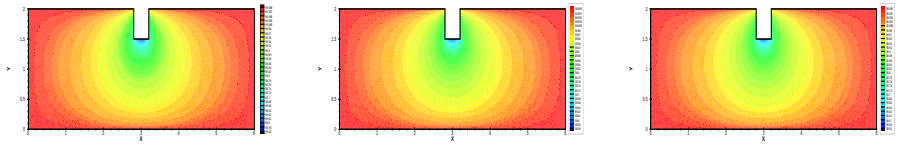

FIGURE 4. Representation of the pressure in the reservoir for $\phi = 10^2$ on $\partial\Omega_p \setminus \Gamma$, $\Delta t = 0.001$, and $T = 5.0$. Left: `T-BE`; Middle: `RPC-BE`; Right: `RPC-BDF2`.

Figure 6, shows that less pressure on the boundary of the reservoir $\phi = 10.0$ supplies smaller amount of fluid, which decreases the magnitudes of the fluid flow in the vertical production wellbore.

In Figure 7-8, we show the unconditional stability of the proposed finite element methods by fixing the temporal step sizes $\Delta t = 0.001$ with varying mesh sizes

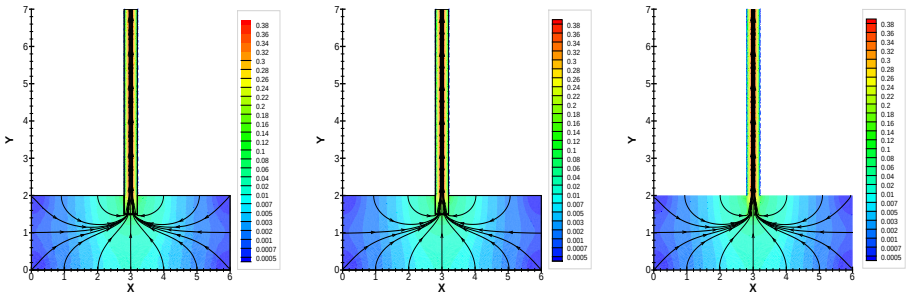

FIGURE 5. The flow speed and streamlines around a vertical production wellbore attatched with a reservoir for $\phi = 10^2$ on $\partial\Omega_p \setminus \Gamma$, $\Delta t = 0.001$ and $T = 5.0$ using $P_2 - P_1 - P_2$ finite elements. Left: `T-BE`; Middle: `RPC-BE`; Right: `RPC-BDF2`.

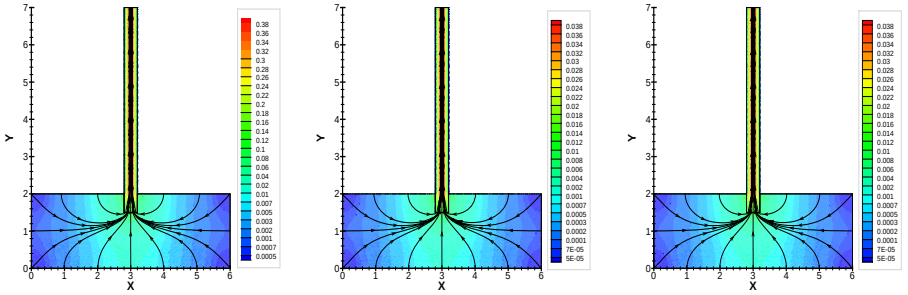

FIGURE 6. The flow speed and streamlines around a vertical production wellbore attatched with a reservoir for $\phi = 10.0$ on $\partial\Omega_p \setminus \Gamma$, $\Delta t = 0.001$ and $T = 5.0$. Left: `T-BE`; Middle: `RPC-BE`; Right: `RPC-BDF2`.

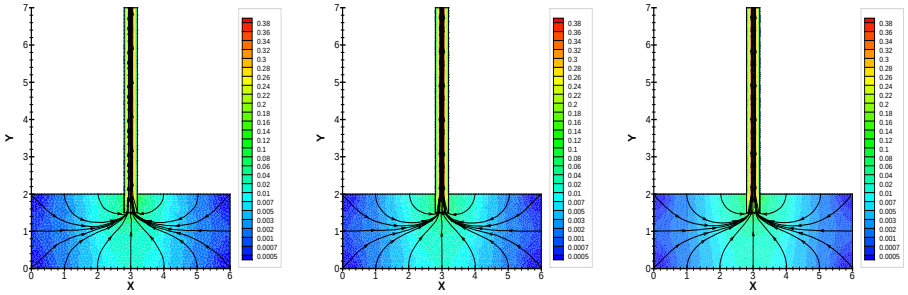

FIGURE 7. The flow speed and streamlines around a vertical production wellbore attatched with a reservoir of the proposed algorithm $\texttt{RPC} - \texttt{BE}$ for $\phi = 10^2$ on $\partial\Omega_p \setminus \Gamma$, $\Delta t = 0.001$ and $T = 5.0$ with different mesh scales. Left: $h_{max} = 0.01$; Middle: $h_{max} = 0.075$; Right: $h_{max} = 0.05$.

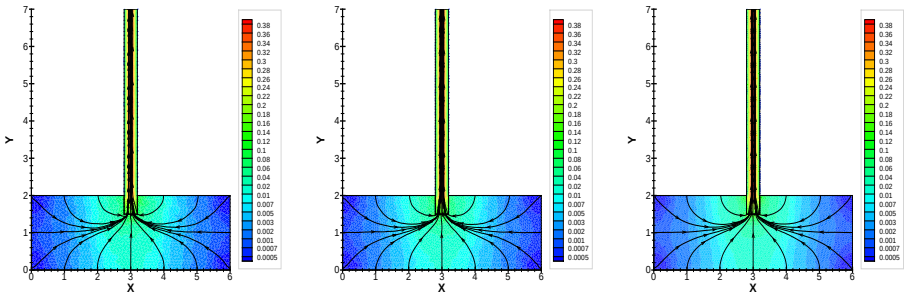

FIGURE 8. The flow speed and streamlines around a vertical production wellbore attatched with a reservoir of the proposed algorithm `RPC-BDF2` for $\phi = 10^2$ on $\partial\Omega_p \setminus \Gamma$, $\Delta t = 0.001$ and $T = 5.0$ with different mesh scales. Left: $h_{max} = 0.01$; Middle: $h_{max} = 0.075$; Right: $h_{max} = 0.05$.

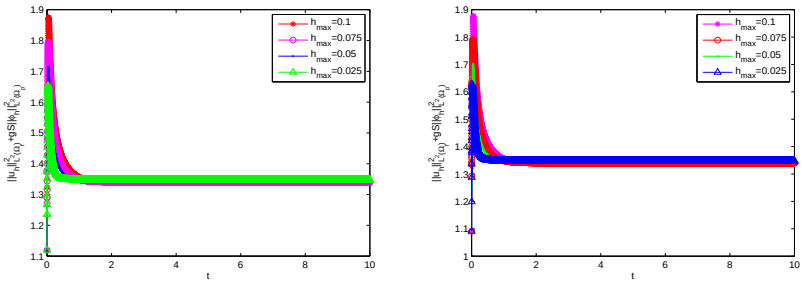

FIGURE 9. 'Energy versus Time' on the time step levels with different mesh sclaes. Left: `RPC-BE`; Right: `RPC-BDF2`.

$h_{max} = 0.1, 0.075$ and 0.05. Figure 9 presents the long-time stability of the proposed `T-BE`, `RPC-BE` and `RPC-BDF2`. Herein we illustrate the energy $\|\mathbf{u}_h\|_{L^2(\Omega_f)} + gS\|\psi_h\|^2_{L(\Omega_p)}$ at a time step level $\Delta t = 0.001$ with the final time $T = 10.0$ by gradually decreasing mesh sizes $h_{max} = 0.1, 0.075, 0.05$, and 0.025, respectively. The numerical results demonstrate that the stability of the proposed methods is independent of the varying mesh sizes and presents the long-time behavior as well.

Theorem 4.7 has a time-step restriction, where we set up the experiment shown in Figure 10. We simulated the effects of different permeability and time steps on the experimental results. In Figure 11, we show the velocity within the calculated region at different permeability. With the increase of permeability, the fluid velocity in the calculated region increases gradually. In Figure 12, we show the long-time behavior of the proposed finite element methods by varying temporal step sizes $\Delta t = 0.001, 0.05$ and 0.1. As the time step increases, the results begin to become unstable. A time-step restriction is necessary for the long-time stability of the system (2.1)-(2.10).

6.3. 3D horizontal wellbore with open hole.

In order to simulate the horizontal wellbore with open hole. Assume that $\Omega_f = [0.1, 0.4] \times [0.2, 0.3] \times [0, 0.5]$ is the free flow region and $\Omega_p = [0, 0.5]^3 \setminus \Omega_f$ is the

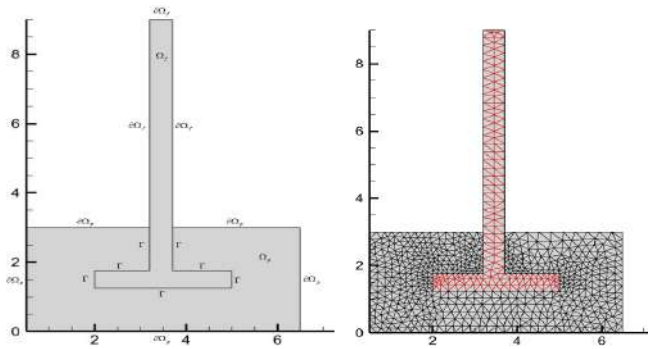

FIGURE 10. Left: the computational domain with free flow region Ω_f and porous media flow region Ω_p; Right: the illustration of the computational mesh.

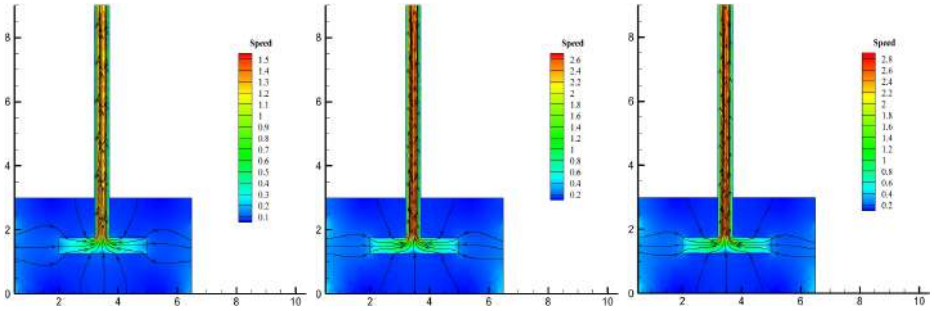

FIGURE 11. The flow speed and streamlines around a production wellbore attatched with a reservoir of the proposed algorithm `RPC-BDF2` for $\phi = 10^4$ on $\partial\Omega_p \setminus \Gamma$, $\Delta t = 0.001$ and $T = 5.0$ with different permeability k. Left: $k = 10^{-12}$; Middle: $k = 10^{-8}$; Right: $k = 10^{-4}$.

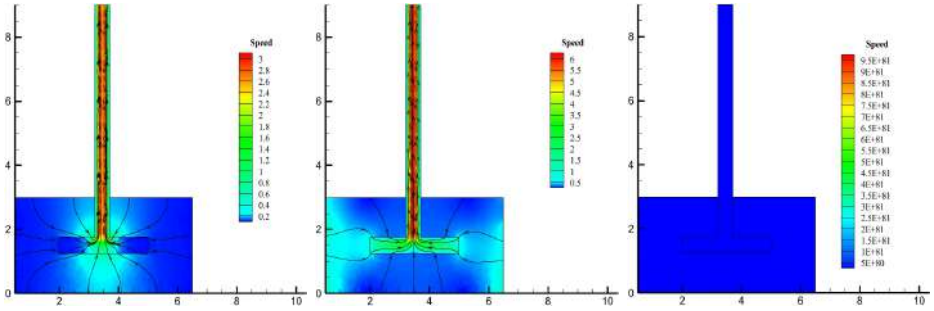

FIGURE 12. The flow speed and streamlines around a production wellbore attatched with a reservoir of the proposed algorithm `RPC-BDF2` for $\phi = 10^4$ on $\partial\Omega_p \setminus \Gamma$ and $T = 20.0$ with different time steps Δt. Left: $\Delta t = 0.001$; Middle: $\Delta t = 0.05$; Right: $\Delta t = 0.1$.

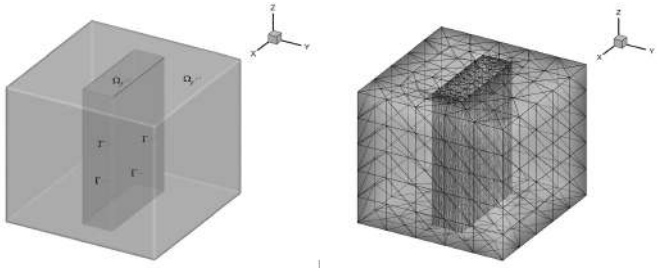

FIGURE 13. Model region and finite element mesh parting

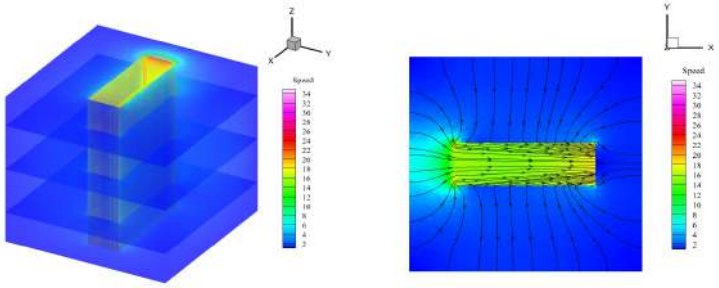

FIGURE 14. The flow speed and streamlines of the proposed algorithm `T-BE`(CPU times=101916s). Left: 3D velocity view; Right: 2D cross section velocity streamline.

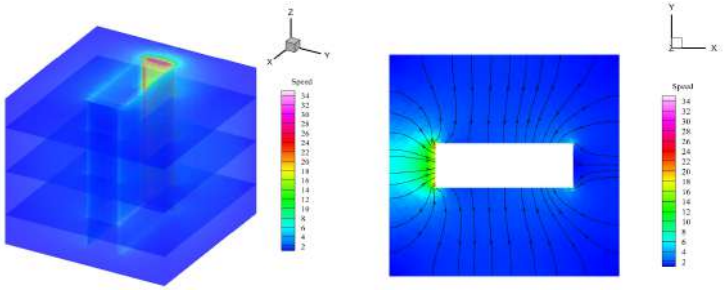

FIGURE 15. The flow speed and streamlines around wellbore of the proposed algorithm `T-BE`. Left: 3D velocity view; Right: 2D cross section velocity streamline.

porous media region. The interface $\Gamma = \Omega_f \cap \Omega_p = [0.1, 0.4] \times \{0.2\} \times [0, 0.5] \cup \{0.4\} \times [0.2, 0.3] \times [0, 0.5] \cup [0.1, 0.4] \times \{0.3\} \times [0, 0.5] \cup \{0.1\} \times [0.2, 0.3] \times [0, 0.5]$ (see Figure 13). In order to obtain the expected results, the interface conditions of this numerical experiment are still used by equations (2.5)-(2.7). In particular, the following conditions are used on interface $\{0.4\} \times [0.2, 0.3] \times [0, 0.5]$: $(-p\mathbb{I} + 2\mu\mathbb{D}(\mathbf{u})) \cdot \mathbf{n}_f = 0$. No-slip boundary condition $\mathbf{u} = 0$ is considered on the boundaries $\partial\Omega_f \backslash \Gamma$ of the open hole. The porous media flow velocity is computed by setting $\mathbf{u}_p = -\mathbb{K}\nabla\phi$. On the boundaries of the porous medium $\partial\Omega_p \backslash \Gamma$, we use constant inflow boundary condition by setting $\phi = 10^2$.

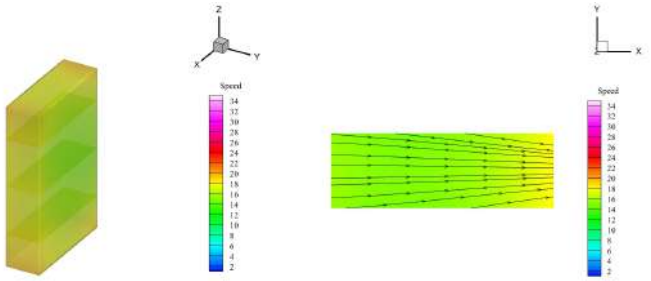

FIGURE 16. The flow speed and streamlines in wellbore of the proposed algorithm `T-BE`. Left: 3D velocity view; Right: 2D cross section velocity streamline.

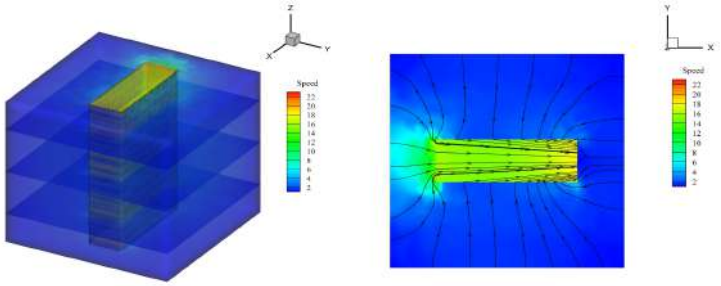

FIGURE 17. The flow speed and streamlines of the proposed algorithm `RPC-BE`(CPU times=80323s). Left: 3D velocity view; Right: 2D cross section velocity streamline.

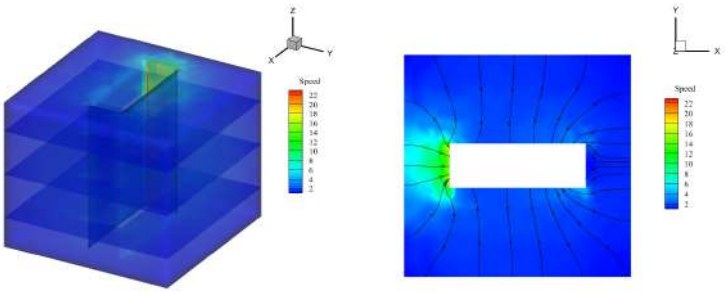

FIGURE 18. The flow speed and streamlines around wellbore of the proposed algorithm `RPC-BE`. Left: 3D velocity view; Right: 2D cross section velocity streamline.

The other parameters value of the model are considered as $\mathbb{K} = k\mathbb{I}, (k = 0.01), S = 10^{-5}, \Delta t = 0.001, T = 3, h = 50$.

From the velocity diagram in Figure 14-19, it can be seen that the fluid in the porous medium can directly enter the wellbore region (free flow region). The fluid velocity increases as it enters the pipe. From the numerical results, the solution results of `RPC-BE` method and `T-BE` method are consistent. In terms of computational efficiency, `RPC-BE` method is more efficient than `T-BE` method. These valid

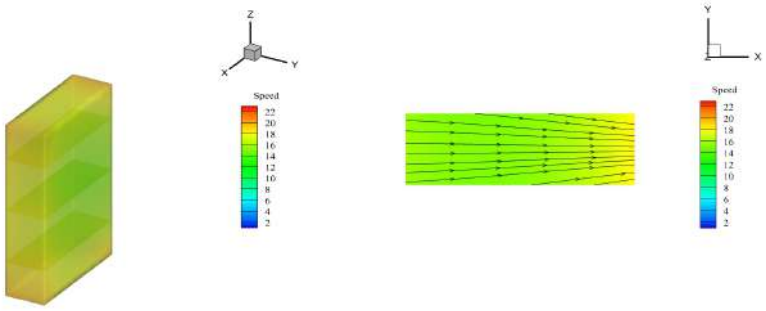

FIGURE 19. The flow speed and streamlines in wellbore of the proposed algorithm `RPC-BE`. Left: 3D velocity view; Right: 2D cross section velocity streamline.

numerical results illustrate the complex dynamic characteristics of the NSD model and further confirm the feasibility of the proposed rotational pressure-correction method.

7. Conclusion

In this article, the rotational pressure-correction scheme for the NSD system is developed and analyzed. The main advantage of this projection method is that it replaces incompressible conditions. The rotational pressure-correction scheme is a special projection algorithm, which distributes the velocity and pressure in different equations. The main algorithm can be completed in two steps. The first step is the viscous step. After the algorithm explicitly processes the pressure gradient, the intermediate velocity can be obtained. The second step is the projection step, which first projects the intermediate velocity onto a divergence-free space, and then corrects the velocity and pressure. In this way, large-scale problems can be transformed into small-scale problems, thus reducing the effort of equation solving. The results of numerical experiments confirm the accuracy of the theoretical analysis, and we can see that the rotational pressure-correction schemes can improve the computational efficiency. Finally, three numerical experiments also verify the applicability of numerical method.

Acknowledgments

Supported in part by NSF of China (No. 11771259), Shaanxi Provincial Joint Laboratory of Artificial Intelligence (No. 2022JC-SYS-05), Innovative team project of Shaanxi Provincial Department of Education(No. 21JP013), and 2022 Shaanxi Provincial Social Science Fund Annual Project (No. 2022D332)

References

[1] T. Arbogast, D. Brunson, A Computational Method For Approximating a Darcy-Stokes system Governing a Vuggy Porous Medium, Comput. Geosci., 11(2007): 207–218.

[2] Y. Cao, M. Gunzburger, X. Hu, F. Hua, X. Wang and W. Zhao, Finite Element Approximation for Stokes-Darcy Flow with Beavers-Joseph Interface Conditions, SIAM J. Numer. Anal., 47(2010): 4239–4256.

[3] N. Chen, M. Gunzburger and X. Wang, Asymptotic Analysis of the Differences Between the Stokes-Darcy System with Different Interface Conditions and the Stokes-Brinkman System, J. Math. Anal. Appl., 368(2010): 658–676.

[4] V. Girault and B. Rivière, DG Approximation of Coupled Navier-Stokes and Darcy Equations by Beaver-Joseph-Saffman Interface Condition, SIAM J. Numer. Anal., 47(2009): 2052–2089.

[5] M. Mu, J. Xu, A Two-Grid Method of a Mixed Stokes-Darcy Model for Coupling Fluid Flow with Porous Media Flow, SIAM J. Numer. Anal., 45(2007): 1801–1813.
[6] L. Badea, M. Discacciati and A. Quarteroni, Numerical Analysis of the Navier-Stokes/Darcy Coupling, Numer. Math., 115(2010): 195–227.
[7] Y. Cao, M. Gunzburger, F. Hua and X. Wang, Coupling Stokes-Darcy Model with Beavers Joseph Interface Boundary Condition, Comm. Math. Sci., 8(2010): 1–25.
[8] A. Cesmelioglu, B. Riviere, Analysis of Time-Dependent Navier-Stokes Flow Coupled with Darcy Flow, J. Numer. Math., 16(2008): 249–280.
[9] M. Cui, N. Yan, A Posteriori Error Estimate for the Stokes-Darcy System, Math. Methods Appl. Sci., 34(2011): 1050–1064.
[10] T. Karper, K. Mardal and R. Winther, Unified Finite Element Discretizations of Coupled Darcy-Stokes Flow, Numer. Methods Partial. Differ. Equ., 25(2009): 311–326.
[11] H. Rui, R. Zhang, A Unified Stabilized Mixed Finite Element Method for Coupling Stokes and Darcy Flows, Comput. Methods Appl. Mech. Engrg., 198(2009): 2692–2699.
[12] Y. Cao, M. Gunzburger, X. He and X. Wang, Robin-Robin Domain Decomposition Methods for the Steady Stokes-Darcy Model with Beaver-Joseph Interface Condition, Numer. Math., 117(2011): 601–629.
[13] W. Chen, M. Gunzburger, F. Hua and X. Wang, A Parallel Robin-Robin Domain Decomposition Method for the Stokes-Darcy System, SIAM J. Numer. Anal., 49(2011): 1064–1084.
[14] M. Discacciati, E. Miglio and A. Quarteroni, Mathematical and Numerical Models for Coupling Surface and Groundwater Flows, Appl. Numer. Math., 43(2002): 57–74.
[15] M. Discacciati, A. Quarteroni, Analysis of a Domain Decomposition Method for the Coupling of Stokes and Darcy Equations, Numerical mathematics and advanced applications, Springer Italia, Milan, 2003: 3–20.
[16] M. Discacciati, A. Quarteroni, Convergence Analysis of a Subdomain Iterative Method for the Finite Element Approximation of the Coupling of Stokes and Darcy Equations, Comput. Vis. Sci., 6(2004): 93–103.
[17] M. Discacciati, A. Quarteroni and A. Valli, Robin-Robin Domain Decomposition Methods for the Stokes-Darcy Coupling, SIAM J. Numer. Anal., 45(2007): 1246–1268.
[18] X. He, J. Li, Y. Lin and J. Ming, A Domain Decomposition Method for the Steady-State Navier-Stokes-Darcy Model with Beavers-Joseph Interface Condition, SIAM J. Sci. Comp., 37(2015): 264–290.
[19] B. Jiang, A Parallel Domain Decomposition Method for Coupling of Surface and Groundwater Flows, Comput. Methods Appl. Mech. Engrg., 198(2009): 947–957.
[20] J. Hou, D. Hu, X. Li and X. He, Modeling and a Domain Decomposition Method with Finite Element Discretization for Coupled Dual-Porosity Flow and Navier-Stokes Flow, J. Sci. Comput., 95(2023): 67.
[21] C. Qiu, X. He, J. Li and Y. Lin, A Domain Decomposition Method with Lagrange Multipliers and Implicit Schemes for the Time-Dependent Navier-Stokes-Darcy Model with Defective Boundary Condition, J. Sci. Comput., 411(2020): 109400.
[22] I. Babuska and G. Gatica, A Residual-Based a Posteriori Error Estimator for the Stokes-Darcy Coupled Problem, SIAM J. Numer. Anal., 48 (2010): 498–523.
[23] G. Gatica, R. Oyarzua and F. Sayas, A Residual-Based a Posteriori Error Estimator for a Fully-Mixed Formulation of the Stokes-Darcy Coupled Problem, Comput. Methods Appl. Mech. Engrg., 200(2011): 1877–1891.
[24] M. Cai, M. Mu and J. Xu, Numerical Folution to a Mixed Navier-Stokes/Darcy Model by the Two-Grid Approach, SIAM J. Numer. Anal., 47(2009): 3325–3338.
[25] J. Connors, J. Howell and W. Layton, Decoupled Time Stepping Methods for Fluid-Fluid Interaction, SIAM J. Num. Anal., 50(2012): 1297–1319.
[26] W. Layton, H. Tran and C. Trenchea, Analysis of Long Time Dtability and Rrrors of Two Partitioned Methods for Uncoupling Evolutionary Groundwater-Surface Water Flows, SIAM J. Numer. Anal., 51(2013): 248–272.
[27] L. Shan, H. Zheng and W. Layton, A Decoupling Method with Different Sub-Domain Time Steps for the Nonstationary Stokes-Darcy Model, Numer. Methods Partial. Differ. Equ., 29(2013): 549-583.
[28] M. Mu, X. Zhu, Decoupled Schemes for a Non-Stationary Mixed Stokes-Darcy Model, Math. Comp., 79(2010): 707–731.
[29] A. Cesmelioglu, B. Riviere, On the Solution of the Coupled Navier-Stokes and Darcy Equations, J. Sci. Comput., 40(2009): 115–140.

[30] C. Dangelo, P. Zunino, Robust Numerical Approximation of Coupling Stokes and Darcys Flows Applied to Vascular Hemodynamics and Biochemical Transport, ESAIM Math. Model. Numer. Anal., 45(2011): 447–476.
[31] G. Kanschat, B. Riviere, A strongly Conservative Finite Element Method for the Coupling of Stokes and Darcy Flow, Math. Comp. J. Comput. Phys., 229(2010): 5933–5943.
[32] B. Riviere, Analysis of a Discontinuous Finite Element Method for the Coupling Stokes and Darcy Problems, J. Sci. Comput., 22/23(2005): 479–500.
[33] B. Riviere, I. Yotov, Locally Conservative Coupling of Stokes and Darcy Flows, SIAM J. Numer. Anal., 42(2005): 1959–1977.
[34] C. Bernardi, T. Rebollo and F. Hecht, Finite Element Discretization of a Model Coupling Darcy and Stokes Equations and Zoubida Mghazli, M2AN Math. Model. Numer. Anal., 42(2008): 375–410.
[35] V. Ervin, E. Jenkins and S. Sun, Coupling Nonlinear Stokes and Darcy Flow Using Mortar Finite Elements, Appl. Numer. Math., 61(2011): 1198–1222.
[36] J. Galvis, M. Sarkis, Balancing Domain Decomposition Methods for Mortar Coupling Stokes-Darcy Systems, Domain decomposition methods in science and engineering XVI, Lect. Notes Comput. Sci. Eng., vol. 55, Springer, Berlin, 2007: 373–380.
[37] Y. Boubendir, S. Tlupova, Stokes-Darcy Boundary Integral Solutions Using Preconditioners, J. Comput. Phys., 228(2009): 8627–8641.
[38] S. Tlupova, R. Cortez, Boundary Integral Solutions of Coupling Stokes and Darcy Flows, J. Comput. Phys., 228(2009): 158–179.
[39] G. Gatica, R. Oyarzua and F. Sayas, Convergence of a Family of Galerkin Discretizations for the Stokes-Darcy Coupled Problem, Numer. Methods Partial. Differ. Equ., 27(2011): 721–748.
[40] S. Khabthani, L. Elasmi and F. Feuillebois, Perturbation Solution of the Coupling Stokes-Darcy Problem, Discrete Contin. Dyn. Syst. Ser. B, 15(2011): 971–990.
[41] H. Liu, P. Huang and Y. He, A Penalty Finite Element Method for the Stationary Closed-Loop Geothermal Model, Int. J. Numer. Anal. Mod., 20(2023): 557–576.
[42] W. Layton, H. Tran and X. Xiong, Long Time Stability of Four Methods for Splitting the Evolutionary Stokes-Darcy Problem into Stokes and Darcy Subproblems, J. Comput. Appl. Math., 236(2012): 3198–3217.
[43] S. Munzenmaier, G. Starke, First-Order System Least Squares for Coupling Stokes-Darcy Flow, SIAM J. Numer. Anal., 49 (2011): 387–404.
[44] W. Peng, G. Cao, D. zhu and S. Li, Darcy-Stokes Equations with Finite Difference and Natural Boundary Element Coupling Method, CMES Comput. Model. Eng. Sci., 75(2011): 173–188.
[45] W. Cai, J. Li and Z. Chen, Unconditional convergence and optimal error estimates of the Euler semi-implicit scheme for a generalized nonlinear Schrödinger equation, Adv. Comput. Math., 42(2016): 1311C-1330.
[46] W. Chen, M. Gunzburger, D. Song and X. Wang, Efficient and Long-Time Accurate Second-Order Methods for the Stokes-Darcy System, SIAM J. Numer. Anal., 51(2013): 2563–2584.
[47] V. Girault, P. Raviart, Finite Element Method for Navier-Stokes Equations: Theory and Algorithms, Springer-Verlag, Berlin, Heidelberg, 1987.
[48] J. Li, Z. Chen, A New Stabilized Finite Volume Method for the Stationary Stokes Equations, Adv. Comp. Math., 30(2009): 141–152.
[49] J. Li, Z. Chen and Y. He, A Stabilized Multi-Level Method of Non-singular Finite Volume Solutions of the Stationary Navier-Stokes Equations in 3-D, Numer. Math., 122(2012): 279–304.
[50] J. Li, Z. Chen, Optimal L^2, H^1 and L^1 Analysis of Finite Volume Methods for the Stationary Navier-Stokes Equations with Large Data, Numer. Math., 126(2014): 75–101.
[51] R. Temam, Navier-Stokes Equations, Theory and Numerical Analysis, Third ed., North-Holland, Amsterdam, 1984.
[52] J. Li, L. Mei and Y. He, A pressure-Poisson stabilized finite element method for the non-stationary Stokes equations to circumvent the infCsup condition, Appl. Math. Comput., 182 (2006): 24–35.
[53] J. Guermond, L. Quartapelle, A Projection FEM for Variable Density Incompressible Flows, J. Comput. Phys., 165(2000): 167–88.
[54] R. Anderson, J. Andrej, A. Barker and et al., MFEM: A Modular Finite Element Methods Library, Comput. Math. Appl., 81(2021): 42–74.

[55] S. Bouaziz, S. Martin, T. Liu, L. Kavan and M. Pauly, Projective Dynamics: Fusing Constraint Projections for Fast Simulation, InSeminal Graphics Papers: Pushing the Boundaries, 2(2023): 787–797.
[56] W. Takahashi, C. Wen and J. Yao, The Shrinking Projection Method for a Finite Family of Demimetric Mappings with Variational Inequality Problems in a Hilbert Space, Fixed Point Theory, 19(2018).
[57] A. Chorin, Numerical Solution of the Navier-Stokes Equations, Math. Comp., 22(1968): 745–762.
[58] J. Guermond, A. Salgado, A Splitting Method for Incompressible Flows with Variable Density Based on a Pressure Poisson Equation, J. Comput. Phys., 228(2009): 2834–2846.
[59] J. Guermond, A. Salgado, Error Analysis of a Fractional Time-Stepping Technique for Incompressible Flows with Variable Density, SIAM J. Numer. Anal., 49(2011): 917–944.
[60] J. Guermond, P. Minev and J. Shen, An Overwiew of Projection Methods for Incompressible Flows, Comput. Methods Appl. Mech. Engrg., 195(2006): 6011–6045.
[61] Y. Wang, S. Li and Z. Si, A Second Order in Time Incremental Pressure Correction Finite Element Method for the Navier-Stokes/Darcy Problem, ESAIM: M2AN, 52(2018): 1477–1500.
[62] Y. Zhang, Stability and Convergence of First Order Time Discrete Linearized Pressure Correction Projection Method for the Diffusive Peterlin Viscoelastic Model, Appl. Numer. Math., 139(2019): 93–114.
[63] J. Shen, On Error Estimates of the Projection Methods for the Navier-Stokes Equations: Second-Order Schemes, AMS: Math. Comp., 65(1996): 1039–1065.
[64] J. Guermond, J. Shen, Velocity-Correction Projection Methods for Incompressible Flows, SIAM J. Numer. Anal., 41(2003): 112–134.
[65] J. Guermond, J. Shen, On the Error Estimates for the Rotational Pressure-Correction Projection Methods, Math. Comp., 73(2004): 1719–1737.
[66] J. Guermond, P. Minev and J. Shen, Error Analysis of Pressure-Correction Schemes for the Time-Dependent Stokes Equations with Open Boundary Conditions, SIAM J. Numer. Anal., 43 (2005): 239–258.
[67] Y. He, J. Shen, Unconditionally Stable Pressure-Correction Schemes for a Linear Fluid-Structure Interaction Problem, Numer. Math. Theor. Meth. Appl., 7(2014): 537–554.
[68] G. Beavers, D. Joseph, Boundary Conditions at a Naturally Permeable Wall, J. Fluid Mech., 30(1967): 197–207.
[69] I. Jones, Low Reynolds Number Flow Past a Porous Spherical Shell, Proc. Camb. Phil. Soc., 73(1973): 231–238.
[70] P. Saffman, On the Boundary Condition at the Interface of a Porous Medium, Stud. Appl. Math., 1(1971): 77–84.
[71] R. Adams, Sobolev Spaces, Academic press, New York, 1975.
[72] J. Li, M. Yao, M. Mahbub and H. Zheng, The Efficient Rotational Pressure-Correction Schemes for the Coupling Stokes/Darcy Problem, Comput. Math. Appl., 79(2020): 337–353.
[73] E. Hairer, G. Wanner, Solving Ordinary Differential Equations II: Stiff and Differential Algebraic Problems, 2nd ed, Springer-Verlag, Berlin, 2002.
[74] Z. Chen, Finite Element Methods and Their Applications, Spring-Verlag, Heidelberg, 2005.
[75] P. Ciarlet, The Finite Element Method for Elliptic Problems, North-Holland, Amsterdam, 1978.
[76] Y. Gao, X. He, L. Mei and X. Yang, Decoupled, Linear, and Energy Stable Finite Element Method for the Cahn-Hilliard-Navier-Stokes-Darcy Phase Field Model, SIAM J. Sci. Comput., 40(2018): B110–B137.
[77] F. Hecht, O. Pironneau and K. Ohtsuka, FreeFEM++, http://www.freefem.org/ff++/ftp/ (2010).

[1]College of Art and Design, Shaanxi University of Science and Technology, Xian 710021, P. R. China
E-mail: 55348990@qq.com

[2]School of Electrical and Control Engineering, Shaanxi University of Science and Technology, Xian 710021, P. R. China
E-mail: gaojw101@163.com

[3]Department of Mathematics, Comilla University, Cumilla, 3506, Bangladesh
E-mail: dipmahbub13@cou.ac.bd

[4]College of Art and Design, Shaanxi University of Science and Technology, Xian 710021, P. R. China
E-mail: chendan@zhengbang.com.cn